Plasma Plume Characterization in an ECRT with Magnetic Arch Configuration

Sacha Huot

Section of Physics
Ecole Polytechnique Fédérale de Lausanne (EPFL)

EP2 Laboratory
Aerospace Engineering Department
Universidad Carlos III de Madrid (UC3M)

Supervisors

Prof. Jaume Navarro-Cavallé & Prof. Mario Merino
& Dr. Marco Inchingolo (UC3M)
Prof. Ivo Furno & Dr. Fabio Avino (EPFL)

Madrid, October 17, 2025



Abstract

This thesis presents the experimental characterization of the plasma plume generated by an electron cyclotron resonance thruster (ECRT) operating in a magnetic arch configuration. The work was conducted at the EP2 Laboratory (UC3M) as part of the ZARATHUSTRA project. The studied prototype consists of two coaxial ECR sources mounted side by side and operated with opposite magnetic polarities, forming an arched magnetic topology that connects both magnetic nozzles. This novel configuration aims to mitigate the large magnetic dipole moment inherent to single-nozzle ECRTs, reduce plume divergence, and enable thrust vectoring.

The native magnetic field topology of the thruster was mapped in three dimensions using a triaxial Hall probe, while the exhaust plasma was diagnosed with Langmuir probes, Faraday cups and RPA. Measurements of plasma potential, floating potential, electron temperature, and density were performed in both the horizontal and vertical planes of the plume under varying operating conditions. The results reveal a highly structured plasma distribution shaped by the magnetic arch, with evidence of asymmetries arising from the magnetic arch topology. Regions of increased electron temperature were observed along the arch, indicating efficient local power deposition and electron confinement. The analysis of magnetic field induced drifts suggests that magnetic topology plays a dominant role in determining cross-field transport and plume confinement.

Overall, the results provide new experimental insight into the physics of clustered ECRT systems and revealed key phenomenons occurring in the presence of a magnetic arch.

Contents

1 Introduction **5**
- 1.1 Motivation . . . 6
- 1.2 Electric propulsion . . . 7
  - 1.2.1 Concept and history . . . 7
  - 1.2.2 Classes of electric propulsion thrusters . . . 7
  - 1.2.3 Propellants . . . 8

2 Theory **9**
- 2.1 Plasma physics . . . 9
  - 2.1.1 Cold plasma . . . 9
  - 2.1.2 The Debye length . . . 10
  - 2.1.3 Ionization energy . . . 11
- 2.2 Electron dynamics . . . 12
  - 2.2.1 Maxwell's equations . . . 12
  - 2.2.2 ECR phenomenon . . . 12
  - 2.2.3 $\vec{B}$ field induced drifts . . . 13
- 2.3 Plasma diagnostics . . . 14
  - 2.3.1 Langmuir probe . . . 14
  - 2.3.2 Faraday cup . . . 15
  - 2.3.3 Retarded Potential Analyzer . . . 16
- 2.4 Electrodeless plasma thrusters . . . 17
  - 2.4.1 Concept and history . . . 17
  - 2.4.2 Electron Cyclotron Resonance Thruster . . . 18
  - 2.4.3 Magnetic nozzle & thrust generation . . . 19

3 Experimental setup & methods **21**
- 3.1 Magnetic Arch Thruster prototype . . . 21
  - 3.1.1 Mechanical assembly . . . 21
  - 3.1.2 Microwave source and transmission line . . . 23
  - 3.1.3 Magnetic arch . . . 24
- 3.2 Thruster magnetic field characterization . . . 24
- 3.3 Vacuum chamber . . . 26
- 3.4 Plasma diagnostics . . . 26
  - 3.4.1 Robotic arm system . . . 26
  - 3.4.2 Plasma diagnostic probes . . . 27
  - 3.4.3 Langmuir probe data processing . . . 28

4 Results & discussion **31**
4.1 Measurements of the $\vec{B}$ field . . . 31
4.1.1 Measurement planes . . . 31
4.1.2 Magnetic field topology . . . 31
4.2 Far-plume measurements . . . 34
4.2.1 Faraday cup measurements . . . 34
4.2.2 Retarded potential analyzer measurements . . . 36
4.3 Langmuir probe measurements in the horizontal plane . . . 41
4.3.1 Full plane characterization . . . 41
4.3.2 Gas flow rate effects . . . 43
4.4 Langmuir probe measurements in the vertical plane . . . 46
4.4.1 Full plane characterization . . . 46
4.4.2 Gas flow rate effects . . . 47
4.5 Plasma asymmetries and $\vec{B}$ field induced drifts . . . 50
4.5.1 Larmor radius . . . 50
4.5.2 $\vec{E} \times \vec{B}$ drift . . . 52
4.5.3 $\nabla \vec{B}$ drift . . . 53
4.5.4 $\vec{B}$ curvature drift . . . 54
4.6 Thermal analysis . . . 55

5 Conclusion **56**
5.1 Outcomes of the work performed . . . 56
5.2 Thruster optimization pathways . . . 57
5.3 Future work on the magnetic arch thruster . . . 57

A Appendix **61**
A.1 DAQ program & hardware . . . 61
A.2 Thermal monitoring . . . 62
A.3 Ceramics degradation . . . 63

Acknowledgment

This master thesis was conducted in the context of the ZARATHUSTRA project, funded by the European Research Council under the grant agreement No 950466.
The results of this thesis have been showcased at the International Electric Propulsion Conference (IEPC) 2025 in London, in the conference paper IEPC-2025-322 [1].

I want to address my gratitude to my supervisors at UC3M, Jaumé Navarro-Cavallé and Mario Merino for welcoming me in the EP2 research group during the thesis and for making it such an exciting journey. Their guidance and teaching were precious.

Thank you to Ivo Furno and Fabio Avino from EPFL for their supervision and the year of TP4 at the SPC which was my first plasma laboratory experience.

I want to thank the EP2 team: Andres, Borja, Davide, Hugo, Guillermo, Inaki, Matteo Ripoli and Matteo Guaita, Elpidio, Tatiana, Omar, Leonardo, Juan for their precious advice and for welcoming me into the life of the lab. A special thank you to Marco Inchingolo for his guidance in the laboratory and his expertise in ECRTs.

I thank Célian Boyé for designing the ECRT prototype used in the thesis and for his availability to answer any questions I had on the prototype.

Lastly, I want to thank my family for their support throughout my studies and my friends Elizabeth, Alejandro, Eric, and Ariane who came to visit in Madrid.







Chapter 1

Introduction

The rapid development of the space industry has led to and is still a driver of innovation in the field of satellite propulsion. The exponential growth of the number of satellites in Earth's orbit [2] shows a growing economical and technological interest in the space industry. This has opened a market for satellite propulsion, where electric propulsion is the dominant technology due to its reliability [3]. As of today, a diversification of the satellite market can be observed, new types of small size satellites emerge [4], mainly for telecommunication purposes. This enables the development of various electric propulsion platforms, tailored to the specific needs of contemporary space missions.
The need for spacecraft propulsion arises from several challenges of space missions: corrective maneuvers to preserve the satellites orbit, de-orbiting at the end of its mission and continuous propulsion for space travel in the case of space probes (DeepSpace1 [5], Smart-1 [6], Hayabusa 2 [7]). Different technologies have been developed to fulfill those needs, the most mature as of today are Hall effect thrusters [8] and ion engines [9], presenting high efficiencies and widespread use across space missions.
The electrodeless plasma thruster (EPT) category is still in the research and development phase, but is a promising technology in terms of power scalability and thruster lifespan, due to elimination of the erosion issues thanks to the electrodeless design [10]. The electron cyclotron resonance thruster (ECRT) is one of the main types of EPT, it relies on the cyclotron resonance of electrons subject to a magnetic field and electromagnetic waves to generate the plasma, which is accelerated and expelled using a magnetic nozzle (MN).
The thruster of interest in this thesis is the ECRT with magnetic arch configuration [11], consisting of an array of two ECRTs with opposite magnetic nozzle polarity. Whereas the clustering of thruster has been realized by Vereen et al. [12] with two helicon plasma thruster in the same magnetic polarity, the magnetic arch configuration is novel and presents several advantages: the cancellation of the net magnetic dipole of the spacecraft which is an inherent issue with single magnetic nozzle thrusters, a reduced plume divergence compared to single ECRTs [13] and the possibility for thrust vectoring. The physics governing the operations of ECRTs and thrust generation inside magnetic nozzles is still a topic of active research and not fully understood. In this context, the experimental study of the exhaust plasma plume of the ECRT with magnetic arch is conducted in hopes to better understand the physics of this type of thruster.
The goals are to determine the native magnetic field generated by the thruster outside of operation as well as measuring basic plasma parameters in the plume such as plasma potential, floating potential, electron temperature and density. This expands and builds upon the work of Boyé et al.[11][14], responsible for the design and creation of the thruster prototype.

1.1 Motivation

The inspiration behind this thesis is the necessity to advance the understanding of electrodeless plasma thrusters and, in particular, electron cyclotron resonance thrusters as a viable alternative to conventional electric propulsion devices. While Hall thrusters and ion engines have reached technological maturity and have already demonstrated their hardness in a wide range of space missions, their long-term operation is still limited by erosion of internal components and power scalability issues. ECRTs, due to their electrodeless design, have the potential to enhance thruster lifetime while enabling high-power operation and can be operated with essentially any propellant. Those advantages make them attractive candidates for next-generation satellite propulsion platforms. Furthermore, the trend of employing multiple thrusters in clusters to meet the requirements of modular, scalable propulsion systems highlights the necessity of investigating the effects arising from clustered geometries. Plume-plume interactions, magnetic field topology, and overlapping electromagnetic wave fields in clustered ECRTs can significantly affect thrust efficiency, ion acceleration mechanisms, and plume divergence. This is particularly relevant to the novel configurations of the magnetic arch topology, where two ECRTs of opposing magnetic nozzle polarity are operated in parallel.
This configuration is very novel in the field of electric propulsion and can be expected to eliminate drawbacks of single magnetic nozzle devices such as large magnetic dipole moments and broad plume divergence while potentially enabling thrust vectoring without moving parts. However, the plasma physics is still not well understood, especially the role of the magnetic topology in confinement and acceleration, and how thruster efficiency scales with clustering. Experimental studies of the exhaust plume of clustered ECRTs are therefore essential to obtain quantitative plasma parameter diagnostics, validation of theoretical and numerical models, and guiding future thruster design. Essentially, the novel magnetic arch configuration is a new concept with little material explaining the physical phenomenons occurring in the arch. Experimental characterization of the full exhaust plume of an ECRT cluster has not yet been performed in the literature. By characterizing fundamental quantities such as plasma potential, floating potential, electron temperature, density, and magnetic field distribution in the plume of a magnetic arch ECRT, this work aims to assist in filling the current knowledge gap and to provide new results directly relevant to the development of scalable, long-life, and high-performance propulsion systems for the fast-evolving satellite industry.

1.2 Electric propulsion

1.2.1 Concept and history

The field of electric propulsion includes the devices and technologies using electrical energy to accelerate propellant at high velocities in order to achieve thrust. Contrary to chemical propulsion, electric propulsion yields lower thrusts but higher propellant exhaust velocities, making the fuel use highly efficient to the detriment of pure propulsive force. Electric propulsion was first theorized by Konstantin Tsiolkovsky and Robert Goddard in the early 20th century [15]. The 1960s saw the development of the technology and the first in space flight of an electric propulsion device in 1964 with the flight of an ion engine aboard the soviet *Zond 1* spacecraft. What started as an experimental and unstable technology is now propelling thousands of satellites, mainly for station keeping, orbit raising and deep space exploration.
The main advantage of electric thrusters is the high exhaust velocity achieved, making them highly fuel efficient compared to chemical rockets. Where a chemical rocket outputs specific impulses in the range of 300 to 450 s, an electric thruster achieves specific impulses in the thousands of seconds. This high fuel efficiency comes at the cost of net thrust, which is several orders of magnitude lower than in chemical rockets. This low thrust is mainly the result of limited electrical power onboard spacecrafts. Due to those characteristics, electric thrusters are best suited for mission where highly efficient, slow and gradual velocity changes are needed. Those being in-space operations or in low earth orbit, where aerodynamic drag is nonexistent or highly limited [16].

1.2.2 Classes of electric propulsion thrusters

Different classes of electric thrusters exist, and can mainly be categorized in 3 groups. The electrothermal thrusters use electricity not to ionize but to heat the propellant through electric resistive heating before expanding it in a nozzle, those technologies include for example the arcjet and resistojet. This category is different from the classical electric thrusters in the sense that electricity is used to heat the propellant rather than to ionize and accelerate it. It can be seen as classical chemical propulsion aided by electrical heating.
The main category is the electrostatic thrusters, which includes the most mature technologies to this date, the ion thruster and Hall effect thruster. In those devices, plasma is generated and the ions are accelerated by a static electric field, applied between electrodes. Ion and Hall thrusters are currently the most widespread technologies on satellites due to their maturity, efficiency and relatively high thrust among electric propulsion devices. The main drawback is the erosion of the electrodes: the accelerating grids for the ion thruster and cathodes for the Hall thrusters, which limits the operating time of the thrusters and power scaling.
The third category is the electromagnetic thrusters that rely mainly on current/magnetic field interactions to accelerate the plasma rather than through an externally applied electric field. Those include magnetoplasmadynamic thrusters, pulsed plasma thrusters and the electrodeless plasma thrusters studied in this thesis (more on those in 2.4).

1.2.3 Propellants

For the most part, excluding the electrothermal thrusters, electric propulsion devices rely on the ionization and acceleration of a propellant material, making the choice of such propellant critical. Different options have been studied and demonstrated from noble gases to metals.
Most state of the art commercially deployed thrusters use noble gases such as Xenon, the most popular propellant. This choice is due to the noble nature of the gas, making it non reactive and simplifying its storage and feeding to the thruster, the high mass of the ions and relatively low ionization energy. However, noble gases in general and especially Xenon are limited in production capacity and highly expensive due to its rarity in air and low yield energy intensive production methods [17]. Some thrusters have been tested to operate with alternative propellant such as Krypton or Iodine, which cheaper and more available but yield lower thrust due to lighter ions. Solid propellants are also employed in in pulsed plasma thrusters as the high current discharges in those devices allow for ionization of solids such as PTFE. Concepts of thrusters for low earth orbit missions experiment air breathing technologies where rarefied earth atmosphere can be used as propellant, potentially removing the need for an onboard propellant tank[18].

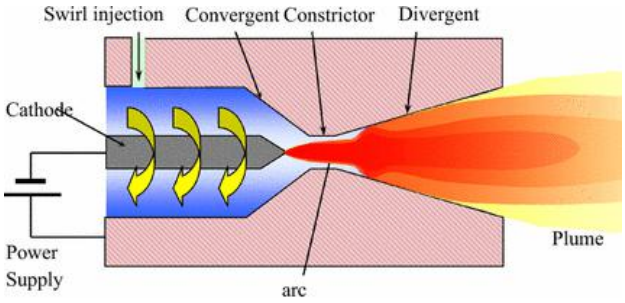

((a)) Arcjet thruster [19].

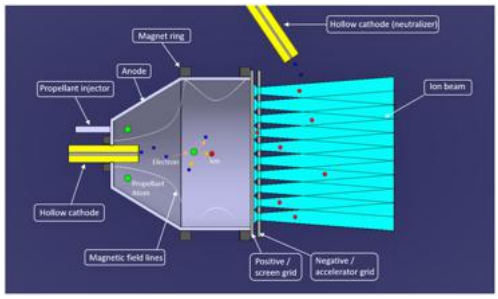

((b)) Gridded ion thruster [20].

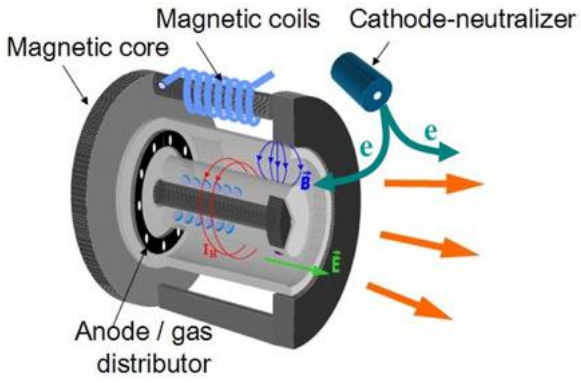

((c)) Hall Effect thruster [21].

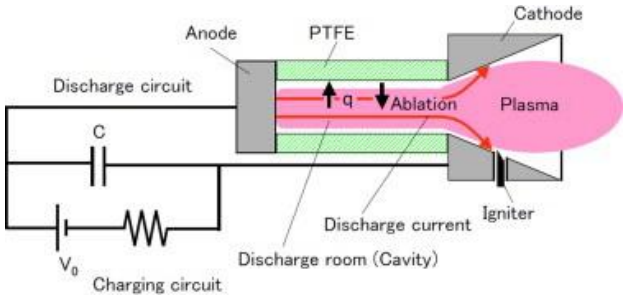

((d)) Pulsed plasma thruster [22].

Figure 1.1: Operating principle schematic of different types of electric propulsion thrusters.

Chapter 2

Theory

2.1 Plasma physics

2.1.1 Cold plasma

A plasma is defined as a quasi neutral, partially or fully ionized gas of unbound charges (electrons and ions) exhibiting collective effects. Characteristic plasma effects are sensibility to electric and magnetic fields, propagation and absorption of electromagnetic waves, quasi infinite electrical conductivity. Plasmas are generated through ionization of neutral atoms, typically in low pressure and high temperature conditions (stars, lightning bolts, tokamaks fusion reactors). Those are referred as hot or thermal plasmas and are characterized by the thermodynamic equilibrium between the heavy positive ions and light negative electrons, meaning that their temperatures T_e and T_i are equal. Generally, thermal plasmas require high temperature and low pressure to exist. However, the thermal equilibrium between electrons and ions is not required for a plasma to exist.

In cold or non-thermal plasma, ions and electron temperatures are different. They are characterized by an electron temperature largely superior to the ions temperature ($T_e >> T_i$). In non-thermal plasmas, if the electron or ion energy distribution deviates from the Maxwell-Boltzmann distribution, the plasma is then called non-Maxwellian.
When it comes to electric propulsion, plasma thrusters operate with cold plasma [16]. The electron and ion temperatures vary depending on the thruster type, model and operating conditions but the ratio between T_e and T_i is generally comprised between ten and several hundreds as displayed in tab.2.1.

Thruster Type	**Electron Temp. (eV)**	**Ion Temp. (eV)**
Ion Thruster	10–30	∼0.1
Hall Thruster	10–50	∼1
Electrodeless Thruster	5–50	<1

Table 2.1: Typical electron and ion temperatures in electric propulsion thrusters. [16] [23]

The temperature difference between ions and electrons is one key aspect of the physics behind electrodeless plasma thrusters, the electron's thermal energy being converted in ions kinetic energy. The physics of EPTs is covered in more details in 2.4.

2.1.2 The Debye length

In order to properly define plasma and especially the condition that it displays collective effects, one has to define the Debye length. It is the characteristic length that measures the screening of one charge carrier's potential by the neighboring charge carriers in the plasma. Contrary to the case of a lone charge carrier in space where the potential decreases with the inverse of the distance r to the charge, a the potential of a charge in a plasma decreases exponentially according to eq.2.1:

$$\phi(r) = \frac{q}{4\pi\varepsilon r} e^{-\lambda_D r} \tag{2.1}$$

where λ_D is the Debye length described by:

$$\lambda_D = \sqrt{\frac{\varepsilon k_B / q^2}{n_e/T_e + n_i/T_i}} \tag{2.2}$$

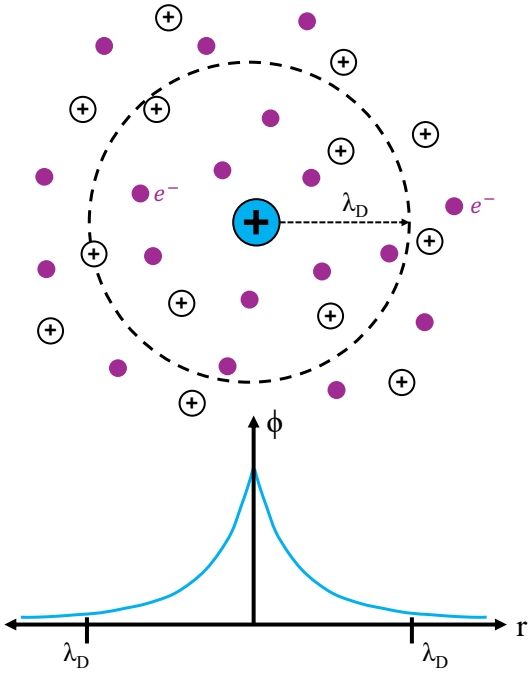

Figure 2.1: Illustration of Debye screening effect (adapted from [24]).

with T_i & T_e the ion and electron temperatures, q the charge, n_i & n_e the plasma species densities, k_B the Boltzman constant and ε the electrical permittivity.
As cold plasma present differences in ion and electron temperatures, the Debye length (eq.2.2) is expressed in its detailed form rather than the classical formula using equal temperature T for both species.
As shown by eq.2.1 and illustrated in fig.3.6, with each Debye length the potential is decreased or screened by a factor e.
The Debye length is key in describing the effects occurring at the boundary of the plasma, where the behavior differs from the bulk of the plasma and quasi neutrality is no longer ensured over length-scales inferior to the Debye length. This becomes relevant for plasma sheath and plays an important role in the theory of Langmuir probes which is described in 2.3.1.

2.1.3 Ionization energy

One of the mechanisms at play in plasma formation is the ionization of the neutral atoms of the gas. This can occur through several ways, either through sheer electrical field force or Coulombian collisions. The latest case covers the inelastic collision of two electrically charged particles interacting in each other's electric field. Those collisions can cause the ionization of the neutral atom provided that the incident particle's kinetic energy is equal or superior to the ionization energy of the atom.

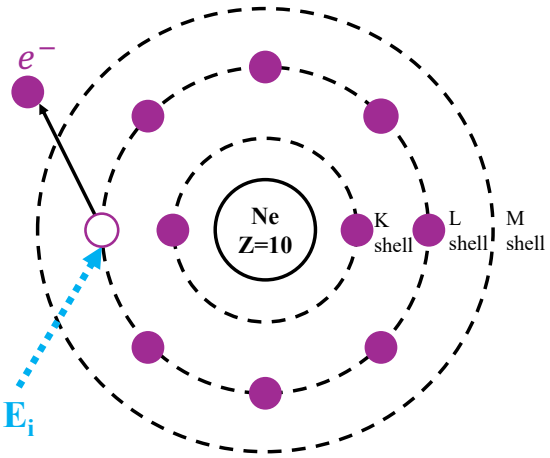

Figure 2.2: Example schematic of the first ionization of a neon atom.

$$E_i + X \rightarrow X^+ + e^- \tag{2.3}$$

This ionization energy E_i is defined as the minimum energy needed to extract an electron from the atom thus turning it into a positive ion. Equation 2.3 describes the ionization process of an arbitrary neutral atom X into the positive ion X^+ by removal of the electron e^-, note that secondary and following ionizations (from X^+ to X^{2+} and so on) can be described in the same way and generally require larger energies than the first ionization. As E_i is the minimum energy to ionize the atom, it intrinsically implies that the most loosely bound electron is to be removed from the outer electron shell. This energy varies with each element and electronic configuration. As a general rule, the ionization energy increases as the outermost electron shell is being filled, with a local maximum for noble gases (full electron shell). For Xenon, the first, second, and third ionization energies are approximately 12.13 eV, 21.21 eV, and 32.12 eV, respectively, illustrating the rapidly increasing difficulty of removing additional electrons once the atom is ionized [25].
The ionization energy is an important quantity as it defines the ease of ionization of a given gas and will condition the choice of the propellant in a plasma thruster, the efficiency of the plasma generation as well as the dimensioning of the required hardware.

2.2 Electron dynamics

2.2.1 Maxwell's equations

As the Maxwell equations are the cornerstone of classical electrodynamics, adding them as a physics reminder is important. They describe the space-time evolution of the electric and magnetic fields and are fundamental to plasma physics. The plasma is a quasi neutral system of charged particles whose dynamics are governed by the external and self generated electromagnetic field.
Maxwell's equations describe the propagation and absorption of electromagnetic waves in the plasma, a phenomenon at the base of plasma generation in an ECRT.

$$\text{Gauss's law:} \qquad \nabla \cdot \mathbf{E} = \frac{\rho}{\varepsilon_0} \tag{2.4}$$

$$\text{Gauss's law for magnetism:} \qquad \nabla \cdot \mathbf{B} = 0 \tag{2.5}$$

$$\text{Faraday's law:} \qquad \nabla \times \mathbf{E} = -\frac{\partial \mathbf{B}}{\partial t} \tag{2.6}$$

$$\text{Ampère–Maxwell law:} \qquad \nabla \times \mathbf{B} = \mu_0 \mathbf{J} + \mu_0 \varepsilon_0 \frac{\partial \mathbf{E}}{\partial t} \tag{2.7}$$

Gauss's law eq.2.4 links charges distribution to the electric field. Gauss's law for magnetism eq.2.5 prevents the existence of magnetic monopoles by setting the magnetic divergence to zero. Faraday's law eq.2.6 describes electric field generation through magnetic field variation in time. Finally, Ampere's induction law eq.2.7 connects currents, magnetic field and time varying electric field, closing the coupling between the electric and magnetic field at the origin of wave propagation.

2.2.2 ECR phenomenon

The plasma thruster studied in this thesis is an electrodeless thruster based on the electron cyclotron resonance to generate the plasma. This ECR phenomenon occurs when electrons are simultaneously subject to a magnetic field and a perpendicular oscillating electric field at the electron cyclotron frequency $f_{ce} = \frac{eB}{m_e c 2\pi}$.
This frequency f_{ce} is the natural frequency at which electrons rotate around the magnetic field lines. It is due to the Lorentz force described in equation 2.8:

$$\mathbf{F} = q(\mathbf{E} + \mathbf{v} \times \mathbf{B}) \tag{2.8}$$

where q is the particle's charge, e in the case of an electron, $\mathbf{E}$ is the electric field, $\mathbf{B}$ the magnetic field and $\mathbf{v}$ the particle velocity.
Solving it in the plane perpendicular to the magnetic field yields a circular rotation whose frequency is the cyclotron frequency f_{ce}.
By applying an oscillating electric field perpendicular to the magnetic field at the cyclotron frequency, the electrons are subject to the conjugated tangential acceleration due the electric field $\mathbf{E}$ and the normal acceleration due to the magnetic field $\mathbf{B}$. The result is an increase in the electron's speed and gyration radius in the plane perpendicular to the magnetic lines.

This increase in electron kinetic energy can be exploited for thruster operations in three ways. First, to efficiently ionize the neutral gas through electron-neutral collisions, the energetic electrons colliding with the neutral atom will ionize the atom if its kinetic energy is superior to the atom's ionization energy. This turns the neutral into an ion plus a new unbound electron, itself being accelerated through ECR and causing further ionization. This process is illustrated in fig.2.3. Second, by efficiently heating the electrons through microwave energy deposition. Lastly, by generating magnetic thrust, this is detailed in 2.4.

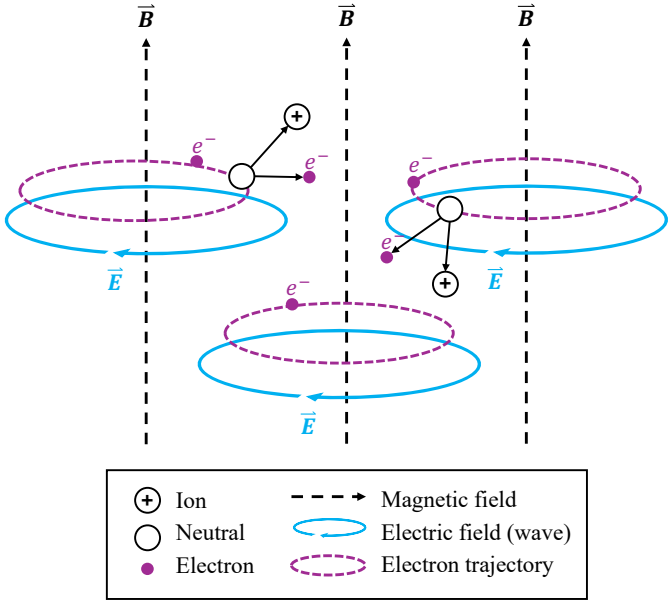

Figure 2.3: Principle schematic of the ECR. (adapted from [26]).

2.2.3 $\vec{B}$ field induced drifts

In a magnetized plasma, charged particles gyrate around magnetic field lines due to the Lorentz force. The circular motion has an associated Larmor radius, which represents the characteristic orbit size of a particle with perpendicular velocity $v_\perp$ in a magnetic field of magnitude B:

$$r_L = \frac{mv_\perp}{|q|B}, \tag{2.9}$$

where m and q are the particle mass and charge, respectively.

When an electric field $\mathbf{E}$ is present perpendicular to $\mathbf{B}$, all charged particles experience a collective $\mathbf{E} \times \mathbf{B}$ drift, independent of their charge or mass:

$$\mathbf{v}_{E\times B} = \frac{\mathbf{E} \times \mathbf{B}}{B^2}. \tag{2.10}$$

Spatial nonuniformities in the magnetic field magnitude also give rise to guiding-center drifts. A gradient in B causes the ∇B drift, arising because particles spend more time on the side of weaker field:

$$\mathbf{v}_{\nabla B} = \frac{mv_\perp^2}{2qB^3}\, \mathbf{B} \times \nabla B. \tag{2.11}$$

Finally, when magnetic field lines are curved, the curvature of the field induces an additional curvature drift, resulting from the centrifugal force on the gyrating particle:

$$\mathbf{v}_c = \frac{mv_\parallel^2}{qB^2}\, \frac{\mathbf{B} \times \boldsymbol{\kappa}}{B}, \tag{2.12}$$

where $\boldsymbol{\kappa} = (\mathbf{b} \cdot \nabla)\mathbf{b}$ is the curvature vector of the magnetic field and $\mathbf{b} = \mathbf{B}/B$ is the unit vector along the field line. These drifts are fundamental to cross-field transport and confinement physics in magnetized plasmas.

2.3 Plasma diagnostics

2.3.1 Langmuir probe

There exists a broad selection of methods and apparatus to measure the parameters of a plasma, this section will only cover the ones used to characterize the plume of the thruster studied in the thesis, namely Faraday cups (FC), Retarded Potential Analyzers (RPA) and Langmuir probes (LP). Langmuir probes are one of the most widespread and basic plasma diagnostic tool, its design is relatively simple and it is able to access several plasma parameters in a single measurement.
It is in practice one or several electrodes, inserted directly inside the plasma, the measurement process consisting in sweeping across a bias range and measuring the current collected by the electrode to obtain an $I - V$ curve. From this curve, several plasma quantities can be extracted: the plasma potential and floating potential, the electron temperature and energy distribution function, as well as the electron and ion density. By nature, a Langmuir probe is an invasive diagnostic method as the conducting electrode is inserted inside the plasma and will inevitably perturb it. In order to properly determine the plasma parameters, the effects of the plasma perturbation by the probe have to be taken into account. Due to their popularity and widespread use, there exists a large literature on the use of Langmuir probes applied specifically to plasma thrusters diagnostics [27] [28].
Langmuir probes can come in different shapes and sizes but the most common designs are either the planar probes or the cylindrical probes. For this thesis, radio frequency (RF) compensated single electrode cylindrical probes are used. They consist in a straight, wire-shaped conducting electrode housed in an insulating (ceramic) tip, aft of the tip is a larger reference electrode used to mitigate the high frequency effects on the probe electrode. The schematic of the Langmuir probe assembly and internal circuit is displayed on fig.2.4

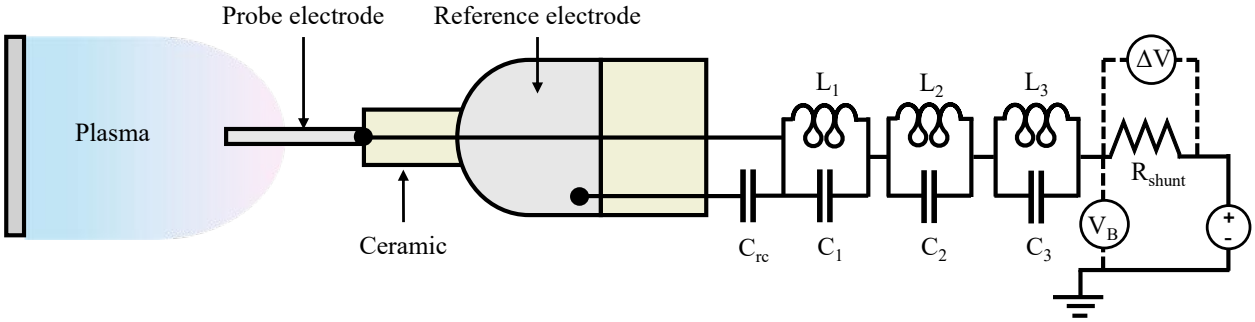

Figure 2.4: Schematic of a RF compensated Langmuir probe (adapted from [27]).

The $I - V$ curve is obtained by biasing the electrode at the voltage V_B, and measuring the current $I = \Delta V / R_{shunt}$. The RF compensation is used to filter the high frequency effects of the radio waves used in certain types of plasma thrusters, RF compensation achieves better performances than simply time averaging the $I - V$ curve over several measurements. It makes use of several LC circuits tuned to the RF frequency and first harmonics. The reference electrode is coupled to those circuits through a capacitance C_{rc} of a few nF [27].
As the thruster studied in this thesis is an ECR operating in the microwave regime (at 2.45 GHz), the frequency is too high to significantly impact measurements [28]. The RF choke system is nonetheless explained since the LP used for the measurements are equipped with it.

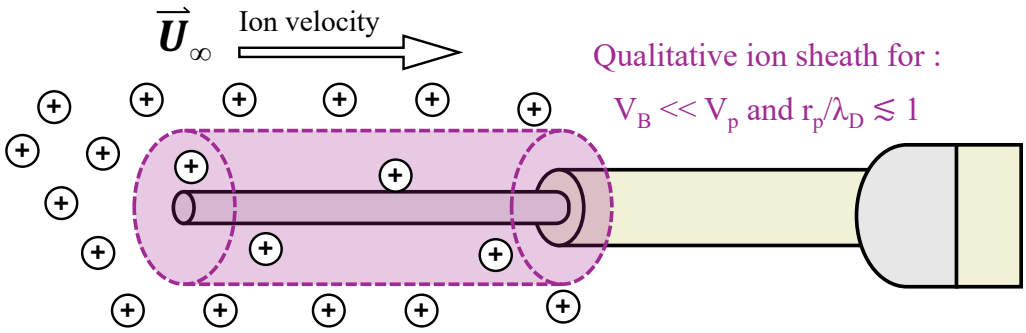

Figure 2.5: Schematic of the sheath expansion along a cylindrical Langmuir probe (adapted from [27]).

As the plasma in electric propulsion devices are generally largely supersonic, literature recommends aligning the axis of a cylindrical Langmuir probe with the flow direction of plasma, in order to mitigate the effects of flowing plasma on the measurement [27]. The reason for this precaution is that the heavy supersonic ions cannot be deflected by a probe unless very large bias voltages are applied. By aligning the probe with the flow, as displayed on fig.2.5 the surface area exposed to the ion flow is minimized, reducing measurement alteration. As the geometry of the plasma plume of the Magnetic Arch Thruster is complex and a priori knowledge of the ions velocity is limited (measured by Boyé using Laser Induced Fluorescence (LIF) in [14]) the alignment is not guaranteed during the experimental campaign.

2.3.2 Faraday cup

The Faraday cup is a relatively simple but robust electrostatic diagnostic device, generally used to measure the flux of charged particles in vacuum. In space propulsion applications, FCs are mainly employed to measure the ion beam current in thruster exhaust plumes. The schematic of its design is illustrated in fig. 2.6. The instrument consists of a grounded metallic housing with a front aperture that defines the acceptance area of the beam. Directly behind the aperture, an electron-suppressor lid is placed; this element is biased to a sufficiently negative voltage (tens to hundreds of volts, depending on the plasma environment) to repel incoming electrons and to prevent secondary electrons from escaping the collector. The central component is the cup collector itself, a metallic electrode connected to a low-noise current measurement circuit that measures the collected ion current.

By design, a basic Faraday cup provides a direct measurement of the collected current, which corresponds to the total charge flux incident on the collector surface. However, it cannot discriminate between ions of different mass or charge state, nor does it provide information on ion energy without additional optics. Error sources in FC measurements include secondary electron emission (electrons ejected from the collector upon ion impact) and ion backscattering (ions reflecting from the collector surface and escaping) both effects typically lead to an artificially reduced measured current.

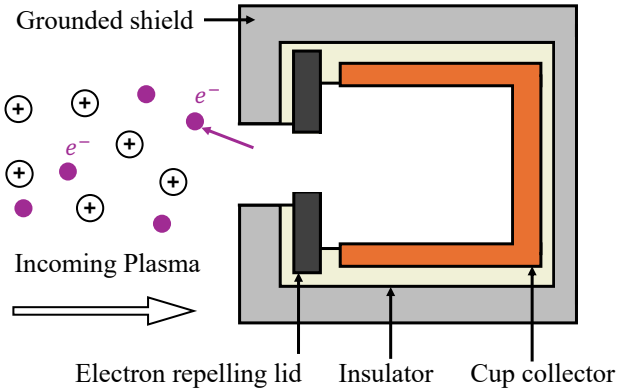

Figure 2.6: Schematic of a Faraday cup (adapted from [29]).

Spatial measurements of thruster exhaust plumes with FC scans enable the reconstruction of ion current density distributions. From these, the total extracted ion current and beam divergence can be estimated, which are directly linked to thruster efficiency and thrust performance [30].

2.3.3 Retarded Potential Analyzer

The Retarded Potential Analyzer is a grid-based electrostatic diagnostic widely employed for measuring the ion energy distribution function (IEDF) in plasma thruster plumes. Its principle of operation relies on selectively repelling ions with a series of biased grids, allowing only ions above a certain kinetic energy to reach the downstream current collector. The design of an RPA consists of three or four aligned mesh grids enclosed in a conductive housing, followed by a metallic current collector. It is illustrated on fig. 2.7.

The entrance grid (G0) is generally kept at the plasma floating potential to minimize perturbations and to shield the downstream biasing fields from the plasma. The second grid (G1) is biased to a sufficiently negative potential to repel the electrons in the incoming plasma and suppress some of the secondary electrons emitted within the analyzer. The discriminator or retarding grid (G3) is biased with a swept positive voltage relative to the plasma, which progressively blocks ions below a given kinetic energy threshold. The fourth optional electron repelling grid (G4) can be added behind the retarding grid and the collector in order to block secondary electrons generated after the first electron repelling grid or at the collector.

A measurement is taken by varying the discriminatory voltage, as it increases, the measured ion current at the collector decreases monotonically: at low voltages all ions are transmitted, while at high voltages only the most energetic ions pass through. The resulting current–voltage ($I^{\smile}V$) curve represents the cumulative IEDF; taking the derivative with respect to the discriminator voltage yields the differential IEDF, which provides detailed information on the energy distributions of the ions. From this data, key plasma properties can be extracted, such as the mean ion energy, ion temperature, effective acceleration potential, and the presence of multiple ion populations. Deviations of the IEDF from Maxwellian or shifted-Maxwellian distributions can indicate plume–plume interactions, potential secondary ion population generated by downstream ionization.

The accuracy of RPA measurements is influenced by engineering factors such as grid transparency, alignment tolerances, field non-uniformities, secondary electron emission, and ion angular divergence. A finite grid spacing leads to fringing fields that distort the energy cutoff, while secondary electron emission from ion impacts may artificially increase the transmitted

current. Similarly, backscattered ions can perturb the measurement.
RPAs complement the use of FCs, by acquiring the IEDF where the FC only measures the raw current, on a practical standpoint, FCs are employed for fast spatial diagnostics, while an RPA measurement can be taken at a specific point of interest.

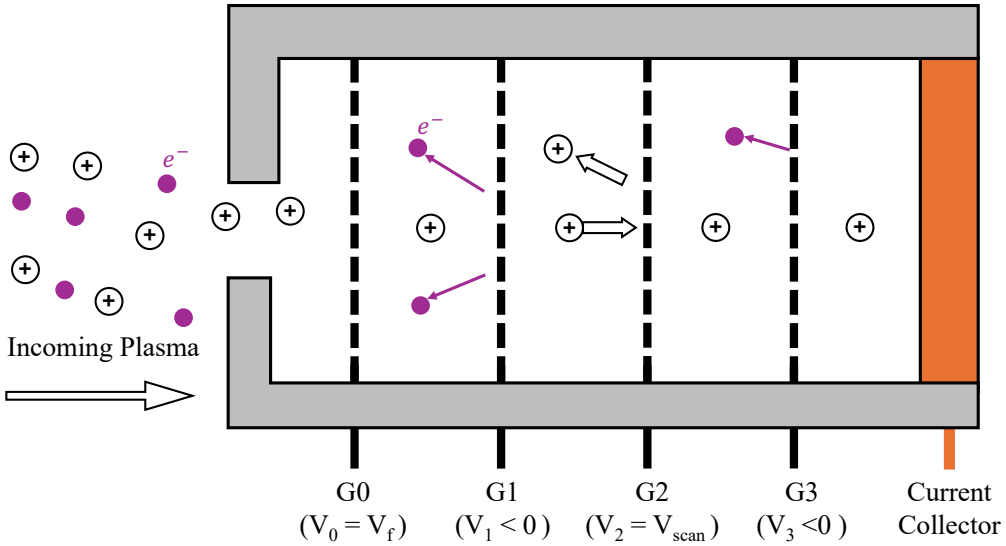

Figure 2.7: Schematic of a Retarded potential analyzer (adapted from [31]).

2.4 Electrodeless plasma thrusters

2.4.1 Concept and history

Expanding upon the general introduction to electric propulsion and the different classes of plasma thrusters mentioned in 1.2, this section presents the details of the the Electrodeless Plasma Thrusters. As their name indicates, those thrusters are characterized by the fact that the plasma is generated and accelerated without being in contact with electrodes, as it would be the case with a gridded ion thruster for example.
The main advantage of this thruster class is the theoretically dramatic reduction in erosion due to plasma/electrode interaction and etching. This can lead to significantly longer lifespan for the thruster and easier power scalability, as the wear rate is not affected by the power setting. This technology saw its beginnings in the 1960s and 1970s with the novel work of Boswell, demonstrating the viability of the helicon discharge for electric propulsion [32].
As those thrusters do not possess electrodes to accelerate the ions, the EPTs generally achieve plasma acceleration through the use of a magnetic nozzle, details of thrust generation processes will be covered in 2.4.3. The interest towards EPTs is growing as space missions requiring prolonged thruster operations develop.



Figure 2.8: Electrodeless plasma thrusters: ONERA's coaxial ECRT (left) [33], UC3M's helicon thruster (right) [34].

2.4.2 Electron Cyclotron Resonance Thruster

The Electron Cyclotron Resonance Thruster (ECRT) is a subcategory of EPTs which relies on the ECR phenomenon described in 2.2.2 to generate the plasma inside the discharge chamber. As mentioned previously, by injecting electromagnetic waves at the electron cyclotron resonance frequency (dependent on the magnetic field strength, in general 2.45 GHz for 875 G) the electrons are heated with high efficiency by the electromagnetic waves and ionize the neutrals, generating and sustaining a high density plasma inside the discharge chamber, compatible with a wide range of gaseous propellants [35].
The designs of ECRTs can vary but rely on a few common elements, illustrated on fig.2.9. The static magnetic field responsible for both the ECR heating and the magnetic nozzle is achieved by permanent magnets, electromagnets (coils) or a combination of both. The microwaves can be injected in the chamber using either a waveguide [36] or a coaxial transmission line with an antenna [37].
As the plasma is essentially generated inside the ECR region, different topologies of the magnetic field inside the plasma chambers are being researched. The use of a diverging magnetic field or magnetic bottle/mirror like topologies influence the confinement of electrons inside the chamber as well as the plasma expansion in the exhaust plume. Current research is carried on the ECR region and magnetic field topology, location inside the chamber and interaction with gas injection location [38], [39], [40]. The results suggest that a thicker resonance region achieved through active (electromagnets) or passive (ferromagnetic component) reduction of the magnetic field gradient leads to improved thrust performances.

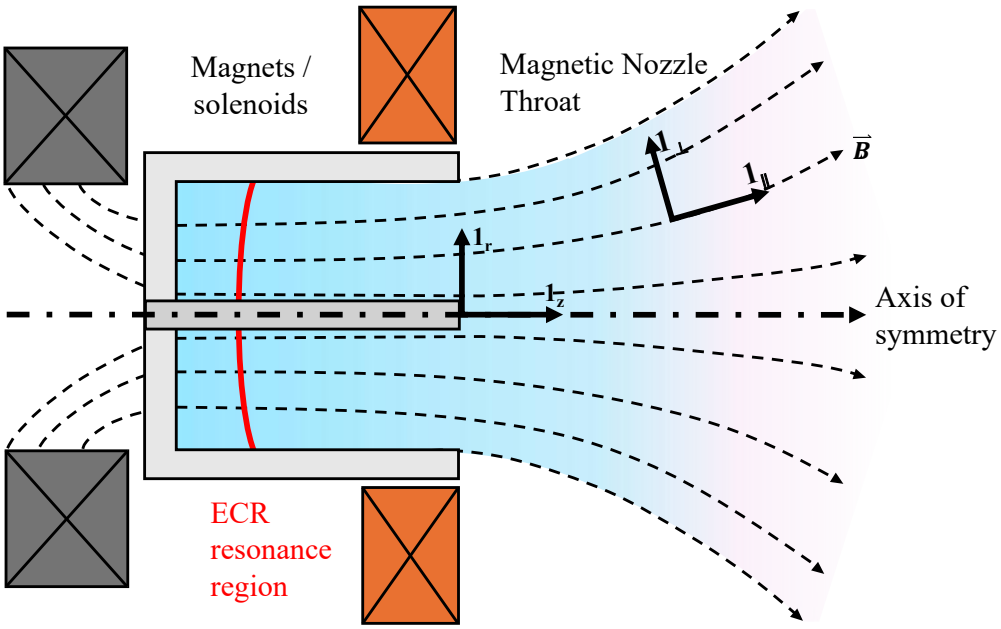

Figure 2.9: Schematic of the design principle of a coaxial ECRT.

2.4.3 Magnetic nozzle & thrust generation

As aforementioned, electrodeless plasma thrusters and thus ECRTs do not rely on any electrode or grid to accelerate the ions and generate thrust. In those devices, the thrust is due to a combination of several phenomenons that are still not fully understood and constitute an active area of research [41].
The magnetic nozzle is the critical element in electrodeless plasma thrusters which acts as the plasma acceleration stage. The nozzle is responsible for guiding the plasma expansion out of the chamber in the exhaust plume. The use of a magnetic nozzle comes with several advantages: limiting plasma-wall interactions through light magnetic confinement, possible thrust vectoring without moving parts through active control of the magnetic field topology, and the removal of the need for a neutralizer as the quasi-neutral plasma as a whole is ejected. However, the nozzle is intrinsically divergent, limiting the thrust efficiency due to cone-shaped ion acceleration. Additionally, the incomplete detachment of the plasma from the streamlines limits the efficiency, especially if a portion of the plasma remains attached to lines reconnecting to thruster, inducing a drag.
Thrust is generated inside the magnetic nozzle following several mechanisms, the main one being the conversion of electron thermal energy into ions directed kinetic energy occurring inside the magnetic nozzle. As the plasma expands downstream of the chamber into the nozzle, the intensity of the diverging magnetic field decreases (increased distance from the magnets) and the electrons which are essentially magnetized in the close plume region experience the magnetic pressure gradient leading to the creation of an ambipolar electric field. This ambipolar field subsequently accelerates the ions downstream, thus generating thrust. This essentially converts the thermal energy of the electrons (several orders of magnitude hotter than the ions) which are highly mobile along the magnetic streamlines, into ion's directed kinetic energy.
A secondary phenomenon is the magnetic thrust illustrated on fig.2.10, due to ECR phenomenon energizing the electrons, a magnetic field is generated by the plasma itself due to the rotational motion of electrons around the magnetic field lines. The resulting magnetic dipole opposes

the dipole of the magnetic nozzle leading to repulsion between the thruster and the plasma and thrust generation. Additionally, the plasma pressure inside the discharge chamber also contributes to thrust by forcing the plasma to escape the chamber, in a fashion similar to gas dynamics. Those last two phenomenon have largely lower contributions to the thrust compared to ambipolar fields.

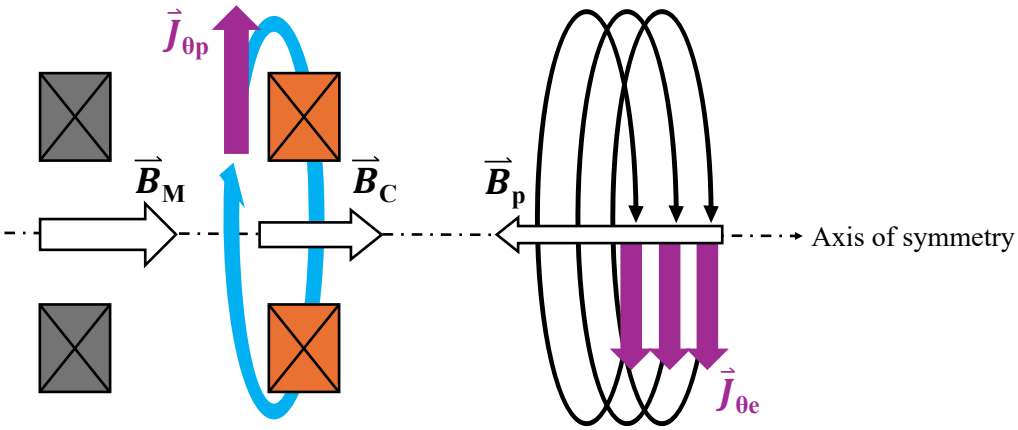

Figure 2.10: Schematic of magnetic thrust generation in an ECRT.

Chapter 3

Experimental setup & methods

3.1 Magnetic Arch Thruster prototype

3.1.1 Mechanical assembly

The Magnetic Arch Thruster used this thesis consists in a cluster of two ECR sources mounted side by side and parallel. In each source, the magnetic field is generated by eight annular N42 permanent magnets mounted together behind the plasma sources and an electromagnet coil mounted around each plasma chamber. The computer assisted design (CAD) model of the thruster and photograph are presented on fig.3.1. The plasma sources are cylindrical chambers (15 mm radius, 20 mm depth), along their axis lays the antenna of the microwave transmission line responsible for the alternating electromagnetic field. The plasma chambers are connected to the DIN7/16 coaxial microwave transmission line by standardized connectors. The plasma sources are in fact the termination of the coaxial line, as their structure is similar to the coaxial cables: the cylindrical chamber plays the role of the outer shield and the antenna acts as the central conductor. Detailed photographs and annotated CAD model are presented on fig.3.2
The propellant gas is axially injected in the chambers through an annular gap between the ceramic backplates separating the chamber from its coaxial connector. Note has to be taken that the gas is initially injected into the annular gap by a radial canal on the side of the chamber. This geometry does not guarantee any uniformity of the gas flow along the annular gap and the gas injection inside the chamber should be considered exempt of rotational symmetry w.r.t the chamber axis. The gas is fed from a single line to the side of both plasma chambers through Teflon tubes and a three way splitter. This configuration of the gas line adds a potential flow imbalance between the chambers.

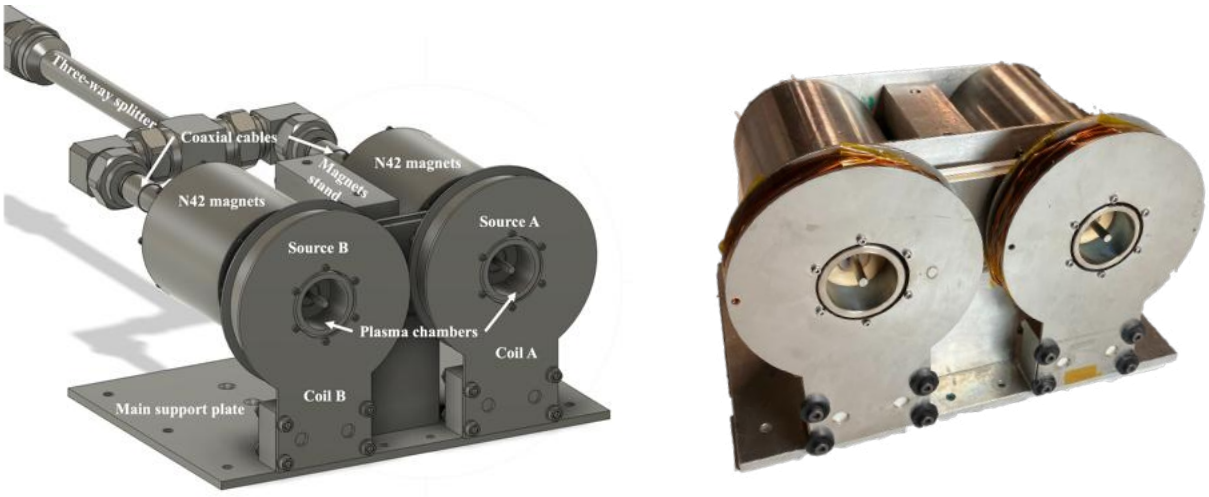

Figure 3.1: Magnetic arch thruster assembly: CAD model (left) and photograph (right).

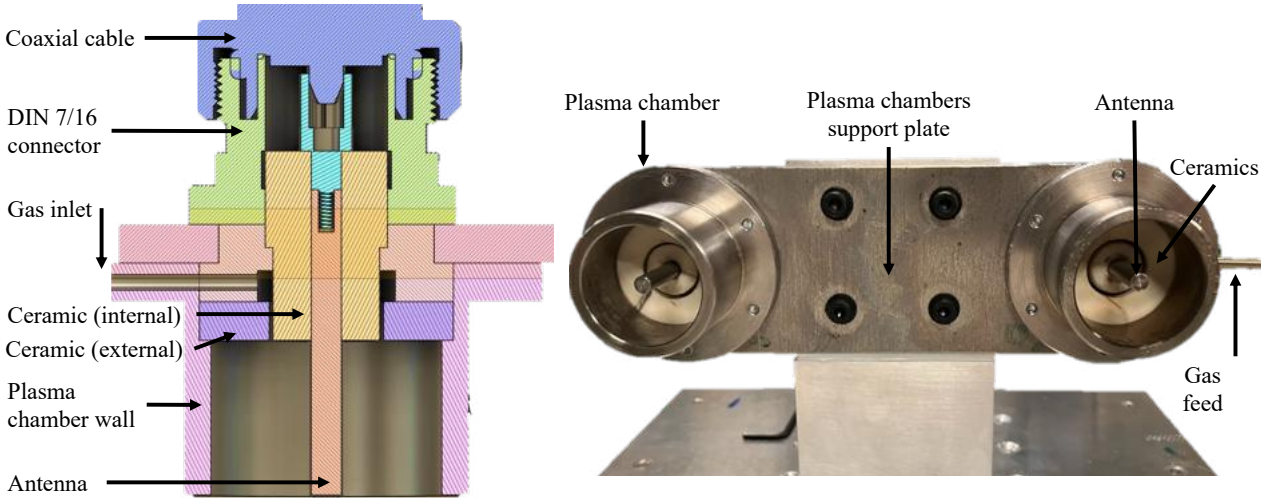

Figure 3.2: Plasma chambers: CAD model horizontal cut view (left) and front view photograph (right), coils are removed for improved visibility.

3.1.2 Microwave source and transmission line

The microwaves are generated by a single solid state microwave generator, model MR1000D-200ML from *Muege* and transmitted to the plasma chambers by a coaxial line. The generator outputs microwaves at a frequency of 2.45 GHz with power from 1 W up to 1 KW. Standard DIN 7/16 coaxial cables are used and a three way splitter allows to separate the line in two terminations to be connected to each source. As the thruster needs to remain electrolytically floating, a DC-block is placed in the transmission line between the generator and the three-way splitter in order to insulate the thruster while transmitting the microwaves. The DC block is a set of two metallic coaxial to waveguide adapters (DIN 7/16 to WR430) facing each other and separated by 1 mm ceramic wafers to ensure insulation. Each component has been checked for transmission and reflection coefficients with a virtual network analyzer (VNA) to guarantee the lowest amount of microwave reflection possible in the transmission line.

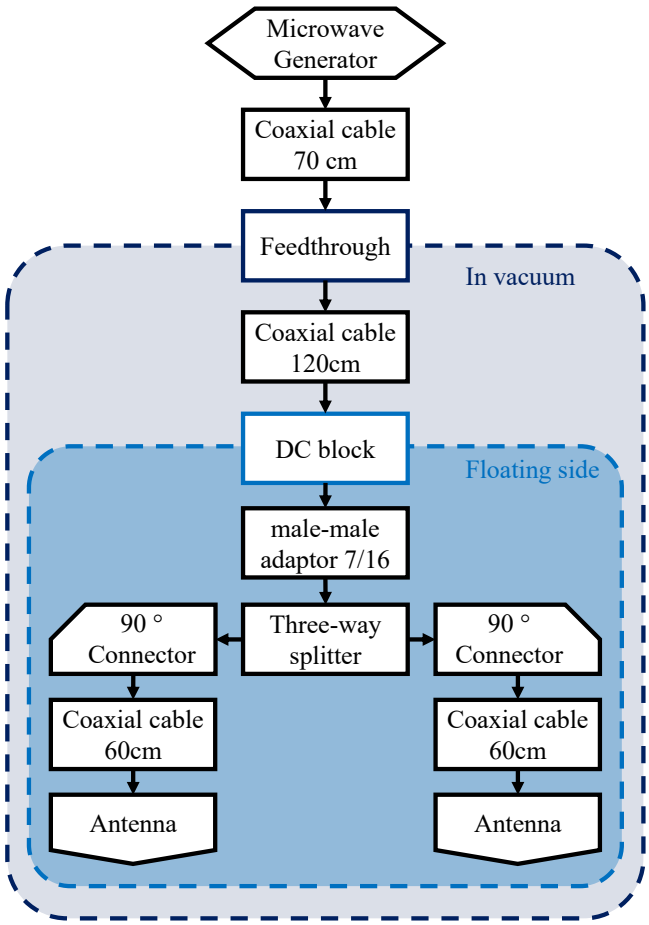

Figure 3.3: Diagram of the microwave transmission line.

The transmission coefficients S_{12} of each component are reported in tab.3.1. Those are obtained by connecting the two terminations of the component to each port of the VNA and comparing the intensity of the signal emitted from the port 1 and received at the port 2. The correspondence between the percentage k of transmitted signal and the loss α in dB is given by $k = 100 \cdot 10^{\alpha/10}$.
The transmission line is not perfect and reflections can occur, which can lead to a standing wave appearing at the junction between two elements of the transmission line. A standing wave can damage the components through heating. In order to avoid damaging components during the experimental campaign, the temperature of the following elements is monitored by thermocouples: feedthrough, three-way splitter, DC block, coaxial cables terminations (for both sources at the antenna side).

Component	Loss (dB)	Transmitted power (%)
Coaxial cable 70 cm	0.23	94.8
Feedthrough	0.22	95.1
Coaxial cable 120 cm	0.29	93.5
DC block	0.19	95.7
Male-Male adapter 7/16	0.04	99.1
Three way splitter (Left)	3.1	49
Three way splitter (Right)	3.02	49.9
90 ° connector (both)	0.03	99.3
Coaxial cable 60 cm	0.33	92.7
Coaxial cable 60 cm	0.28	93.8

Table 3.1: Transmission characteristics of the microwave line components.

3.1.3 Magnetic arch

The main characteristic of the thruster studied is its "Magnetic Arch configuration" which is achieved when a cluster of two ECRTs have opposite magnetic polarities. In this case, the shape of the magnetic nozzle completely differs from the classic single source ECRT configuration. Instead of expanding in a conical shape, the field lines bend in the shape of an arch and connect the two magnetic poles together. As the plasma chamber are coaxial to the magnets and the field is supposed symmetric, streamlines originating from one source's edge connect to the other source.
The Magnetic Arch configuration is achieved by simply having the magnets mounted in opposite polarities to one another and wiring the electromagnets accordingly (to strengthen each sources field). The use of the electromagnet coils is necessary to achieve ignition as the necessary 875 G resonance is located outside (upstream) of the plasma chambers when the coils are turned off. This configuration has the advantage of canceling the thruster net magnetic dipole while adding complexity to the plume configuration and magnetic nozzle effects.

3.2 Thruster magnetic field characterization

In order to precisely measure the magnetic field generated by the permanent magnets and additional electromagnets, a 3-axis Hall effect Gauss probe is used, model 460 3-channels Gaussmeter from *Lake Shore Cryotronics*. This device allows for the measurement of the magnetic field along the 3 directions (x, y, z) simultaneously.
As its name suggests, the Hall effect Gauss probe relies on exploiting the Hall effect to measure the magnetic field. The Hall effect describes the apparition of a transverse voltage across a conductor carrying a current in the presence of a perpendicular magnetic field. This effect appears because the charge carriers (electrons) in the conductor are subject to the Lorentz force. The electrons traveling along the direction of the current are deviated in the perpendicular direction due to the magnetic field orthogonal to the conductor. This deviation causes a charge unbalance across the conductor, thus creating an electric field and a potential difference. The Hall effect schematic and a photograph of the probe are presented on fig.3.4

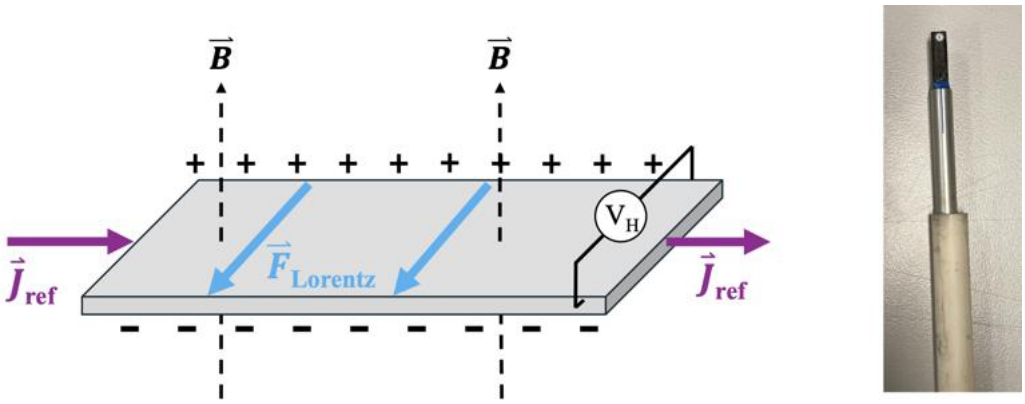

Figure 3.4: Hall effect illustration (right) and tip of the Gauss probe (right).

The magnetic field generated by the permanent magnets and the coils is measured in the exhaust region in front of the thruster and inside each plasma chamber using the Gaussmeter in combination with a 3 degree of freedom robotic arm developed in house at the EP2 laboratory. This allows for a high accuracy scan of the field, with a tunable mesh size. The mesh used is cartesian and the step size is adapted as a function of the distance to the thruster. Inside the two plasma chamber, the mesh is fine with a step size of 4 mm, in the close exhaust the step size is increased to 15mm, and in the far field to 40 mm and further away to 50 mm. The 3D mesh is provided in fig.3.5.

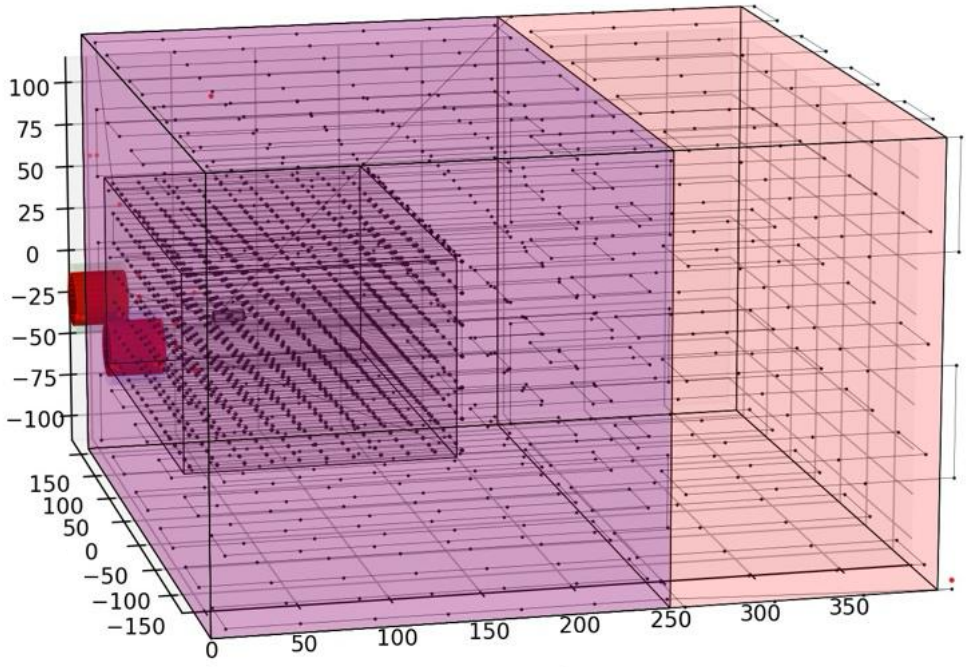

Figure 3.5: Magnetic field measurement mesh. The red cylinders represent the plasma chambers, the colored boxes indicate different mesh accuracies, each black dot is a measurement point.

3.3 Vacuum chamber

The magnetic arch thruster was tested in the large vacuum chamber of the EP2 laboratory at the Universidad Carlos III de Madrid. The large chamber is 3.5 m long, 1.5m in internal diameter, built and certified by *Leybold Oerlikon*. The vacuum is ensured with 2 magnetically levitated turbomolecular pumps and 3 cryopanels, specially optimized for pumping thruster propellants such as Xenon or Krypton. During thruster operations, the pressure is stable in the range of $5 \cdot 10^{-5}$ mbar, for a Xenon mass flow rate of 5 to 20 sccm. The chamber's characteristics are summarized in tab.3.2.



Figure 3.6: Vacuum chamber model S XTT [42].

Vacuum Characteristics		
Total pump capacity	Ultimate pressure	Continuous operations pressure
37000 L·s^{-1}	$< 10^{-7}$ mbar	$< 2 \cdot 10^{-5}$ mbar
Pumps Characteristics		
Roughing pump (1)	Turbo pumps (2)	Cryopanels (3)
Leyvac LV80 (22.3 L·s^{-1})	*MAGW2.200iP* (2000 L·s^{-1})	*Leyvac 140 T-V*

Table 3.2: Large vacuum chamber characteristics

3.4 Plasma diagnostics

3.4.1 Robotic arm system

All the probes used inside the vacuum chamber (Faraday cup, RPA, Langmuir probes) for the characterization of the plasma plume are mounted on a 2 degrees of freedom robotic arm system. This arm system is placed downstream of the thruster inside the vacuum chamber and its position (w.r.t. the vacuum chamber) is adjustable. The arm is capable of azimuthal and radial motion in the horizontal plane, at a fixed height setting. The azimuthal motion has a range of $\theta = \pm 90°$, the radial motion has a range of $r \in [0, 400]$ mm. The arm system is designed to measure the typical conical expansion of the plumes produced by single source thrusters: helicons, Hall effect thrusters and single source ECRTs. Due to the double source nature of the magnetic arch thruster, it is not possible to align the arm system with each of the two sources. The choice has been made for all measurement campaigns to align the center of the azimuthal rotation axis with the origin of the thruster (i.e. the middle point between the two antenna tips) this allows to scan a symmetrical portion of space and conserve the same angle offset w.r.t. both sources, while sacrificing single source alignment. The arm system is represented on fig.3.7 and a photograph of the alignment is provided on fig.3.8.

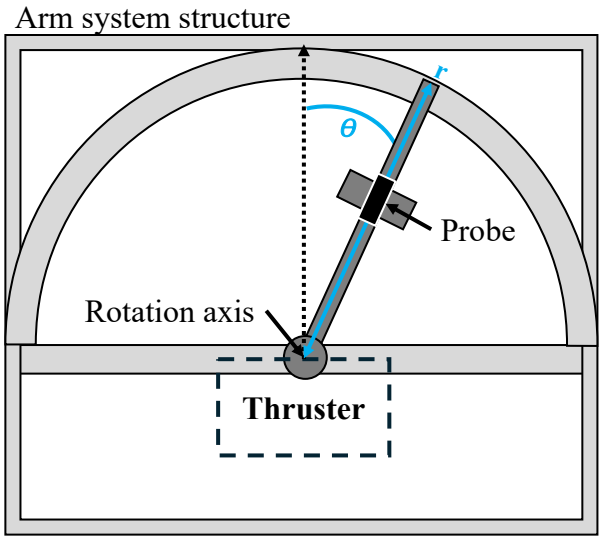

Figure 3.7: Schematic of the 2 degrees of freedom arm system.

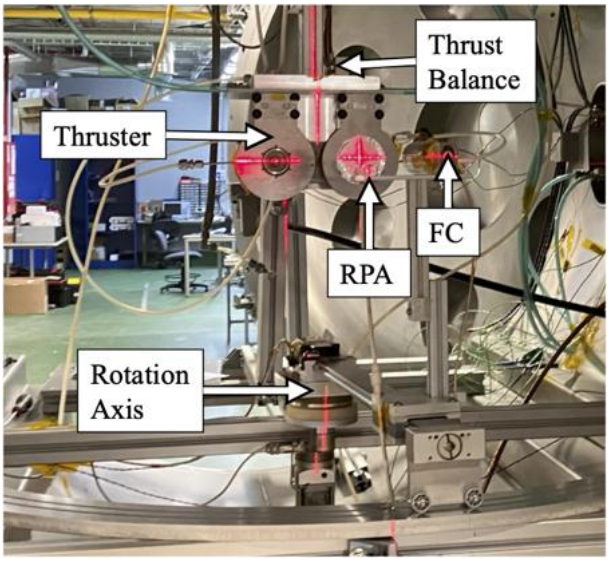

Figure 3.8: Alignment of the probes with the thruster origin.

3.4.2 Plasma diagnostic probes

The Faraday cup used for measurements is built in house. It is equipped with a circular aperture with a radius of 5 mm. The ion current is measured by a high resistance electrometer, model 6517B from *Keithley*.

The retarded potential analyzer is the only probe that is not built in house, model Semion RFEA from *Impedans*. The probe cable and electrometer are part of the same system, no other component is required.

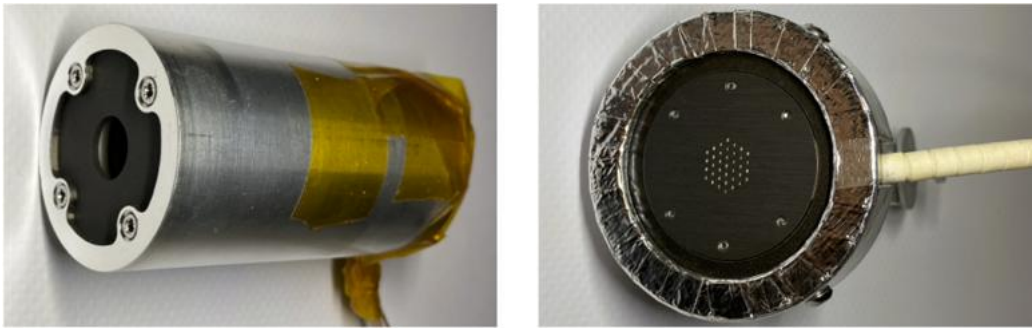

Figure 3.9: Photograph of the Faraday cup (left) and Retarded potential analyzer (right).

A single Langmuir probe model is used and displayed in fig.3.10. The probe is built in-house by the EP2 Laboratory, with a radio frequency damping system as described in 2.3.1, which does not impact measurements for microwave frequency plasma.
The probe electrode is 3 mm in length and 0.254 mm in diameter, with a reference electrode of 4 cm^2. The probe bias voltage is controlled by a high resistance electrometer, model 6517B from *Keithley* with a current resolution of 1 nA and voltage resolution of 50 mV. The acquisition of the $I - V$ curve is automated via a LabVIEW program.

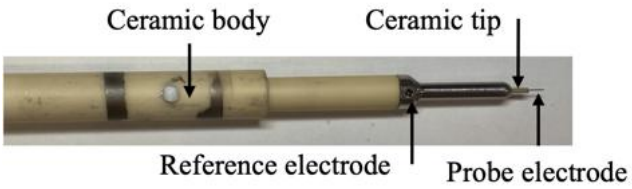

Figure 3.10: Photograph of the Langmuir probe.

3.4.3 Langmuir probe data processing

The $I-V$ curves obtained using Langmuir probes are preprocessed using the method described by Lobbia and Beal in [27] to extract the plasma parameters. The method is shortly described in this section and was automatized using a Python script developed by the author.
Starting from the raw $I-V$ curve, the first quantity identified if the floating potential V_f defined as the bias voltage V_B for which the measured current $I(V_B)$ is closest to 0 A.

$$V_f = \text{argmin } (\text{abs } (I(V_B))) \tag{3.1}$$

A linear fit is applied to the current for voltages V below V_f and the resulting curve is defined as the ion saturation curve (over the whole voltage range).

$$I_{i,sat}(V_B) = a_i V_B + b_i \tag{3.2}$$

The electron current I_e is then obtained by subtracting the ion saturation curve from the total measured current over the whole voltage range.

$$I_e(V_B) = I(V_B) - I_{i,sat}(V_B) \tag{3.3}$$

The plasma potential V_p is then defined as the inflection point of the electron current. This is equivalent to the voltage for which the electron current derivative is maximum. Due to potentially noisy $I-V$ curves, a smoothing can be applied to the electron current before identifying the plasma potential. In the rare case where a curve is too noisy, the plasma potential is manually selected to match the eye-observed inflection point.

$$V_p = \text{argmax } \left(\frac{\mathrm{d}I_e(V_B)}{\mathrm{d}V_B} \right) \tag{3.4}$$

The electron temperature T_e can then be computed as the inverse of the average slope of the linear region of the logarithm of the electron current between the floating and plasma potential.

$$T_e = \left(\left. \frac{\mathrm{d}\ln(I_e(V_B))}{\mathrm{d}V_B} \right|_{V_f<V_B<V_p} \right)^{-1} \tag{3.5}$$

Once T_e is known, the electron density n_e and preliminary ion density are computed as:

$$n_e = \frac{I_e(V_p)}{eA_p}\sqrt{\frac{2\pi m_e}{eT_e}} \quad , \quad n_{i,provi} = -\exp\left(\frac{1}{2}\right)\frac{I_{i,sat}(\min(V_B))}{eA_p}\sqrt{\frac{m_i}{eT_e}} \tag{3.6}$$

where $m_e = 9.11 \cdot 10^{-31}$ kg is the electron mass, $e = 1.6 \cdot 10^{-19}$ C its charge, $m_i = 2.18 \cdot 10^{-25}$ kg the Xenon ion mass (assuming single charged) and A_p the probe area.

The Debye length λ_D is then computed using the electron temperature and preliminary ion density.

$$\lambda_D = \sqrt{\frac{\epsilon_0 T_e}{n_{i,provi} e}} \tag{3.7}$$

with $\epsilon_0 = 8.85 \cdot 10^{-12}\mathrm{F{\cdot}m^{-1}}$ the electrical permittivity of vacuum.
The ratio between the probe's radius and the Debye length r_p/λ_D is computed. A correction on the ion density and ion saturation current is applied based on this ratio:

- No correction is applied if the ratio is superior to 50 (thin sheath regime).
- If the ratio is between 50 and 3, the transitional sheath theory applies and the ion density is adjusted according to:

$$\begin{aligned} n_i &= \frac{1}{aAp}\sqrt{2\pi m_i} e^{-3/2} T_e^{b-1/2} \left(-\frac{\mathrm{d}I(V_B)^{1/b}}{\mathrm{d}V_B}\bigg|_{V_B<V_f} \right)^b \\ a &= 1.18 - 0.0008\left(\frac{r_p}{\lambda_D}\right) \quad b = -0.0684 + \left(0.722 + 0.928\left(\frac{r_p}{\lambda_D}\right)\right)^{-0.729} \end{aligned} \tag{3.8}$$

- If the ratio is inferior to 3, the orbital motion limited (OML) sheath theory applies and ion density is corrected according to eq.3.8 with $a = 2/\sqrt{\pi}$ and $b = 1/2$.

If a correction was applied, either transitional or OML sheath, the method is repeated from eq.3.3 with an updated ion saturation current $I_i(V_B)$ replacing $I_{i,sat}(V_B)$ (according to eq.3.9) until convergence is achieved. This usually takes between 3 and 5 iterations.

$$\begin{aligned} I_i(V_B) &= eA_p n_e \sqrt{\frac{eT_e}{2\pi m_i}} a \left(\frac{Vp - V_B}{T_e}\right)^b \text{ , for a transitional sheath, } a \text{ and } b \text{ from 3.8.} \\ I_i(V_B) &= \frac{eA_p n_e}{\pi}\sqrt{\frac{2e(V_p - V_B)}{m_i}} \text{ , for an OML sheath.} \end{aligned} \tag{3.9}$$

The electron distribution function (EEDF) can also be computed from the electron current according to:

$$f(\epsilon = V_p - V_B) = \frac{2}{e^2 A_p}(2m_e\epsilon)^{1/2}\frac{\mathrm{d}^2 I_e}{\mathrm{d}\epsilon^2} \tag{3.10}$$

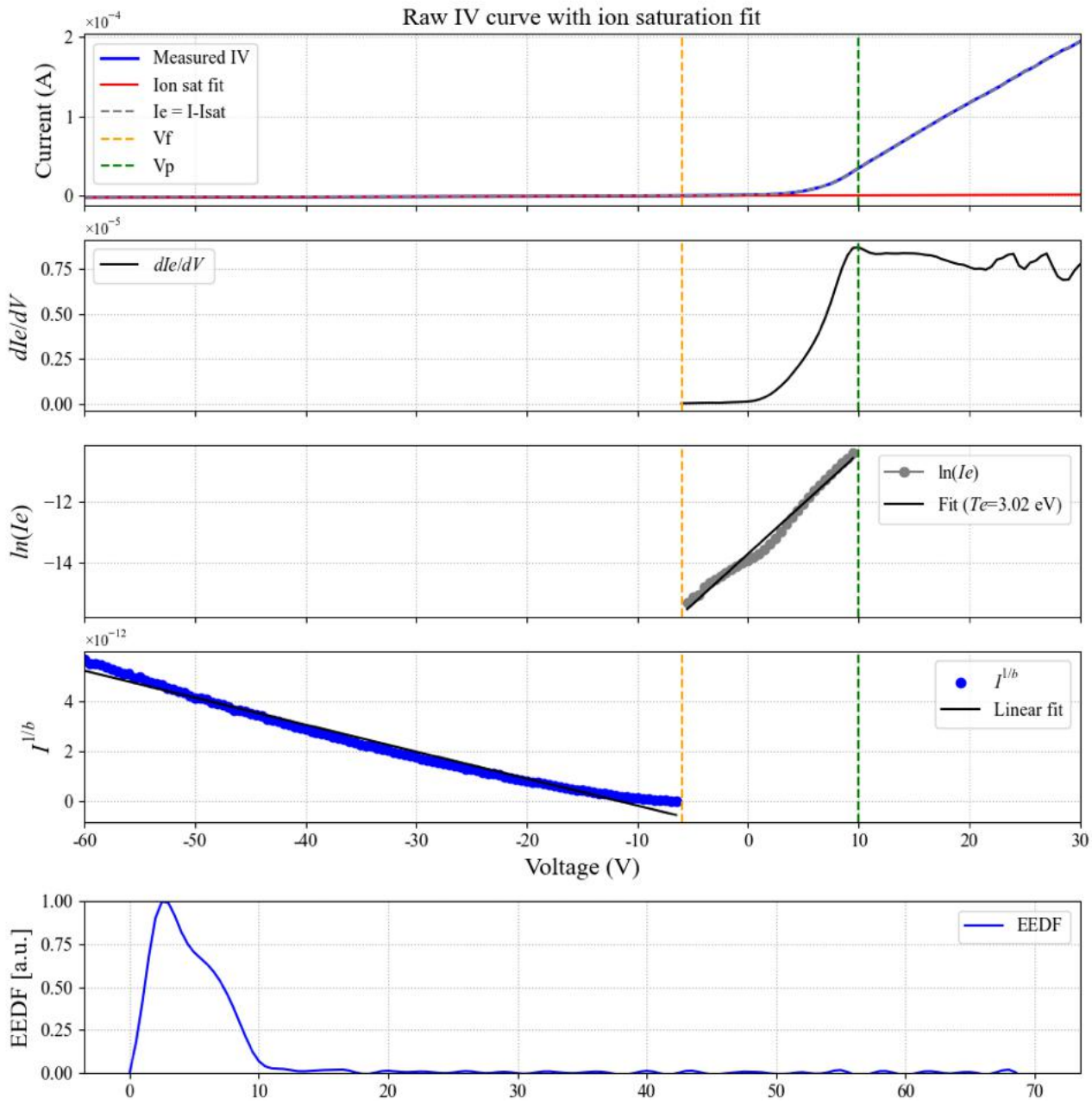

Figure 3.11: $I - V$ curve postprocessing example. Top to bottom: raw signal with computed ion saturation and electron current, plasma potential identification, electron temperature and ion density identification with linear fits, EEDF.

The example shown in fig.3.11 graphically illustrates the computations performed to post process an $I - V$ curve from a Langmuir probe. Note that the model used to post process the curves assumes a Maxwellian distribution of the electrons, this is not always the case in practice, especially inside the magnetic arch. This can be seen on the EEDF and the third subplot of fig.3.11, where the trend is not strictly linear, yet a linear fit is performed according to the Maxwellian assumption. The EEDF shows a non gaussian shape, with a secondary peak, suggesting two electron populations.

Chapter 4

Results & discussion

4.1 Measurements of the $\vec{B}$ field

4.1.1 Measurement planes

In all of the experiments performed on the thruster, measurements were taken in one of two planes. The first is the exhaust or horizontal plane, which contains the magnetic arch and both plasma sources. The second is the symmetry or vertical plane which cuts in the center of the magnetic arch, in between the two sources. Both planes are represented on fig.4.1, along with the thruster origin (center of the line connecting both antenna tips) and the coordinate system.

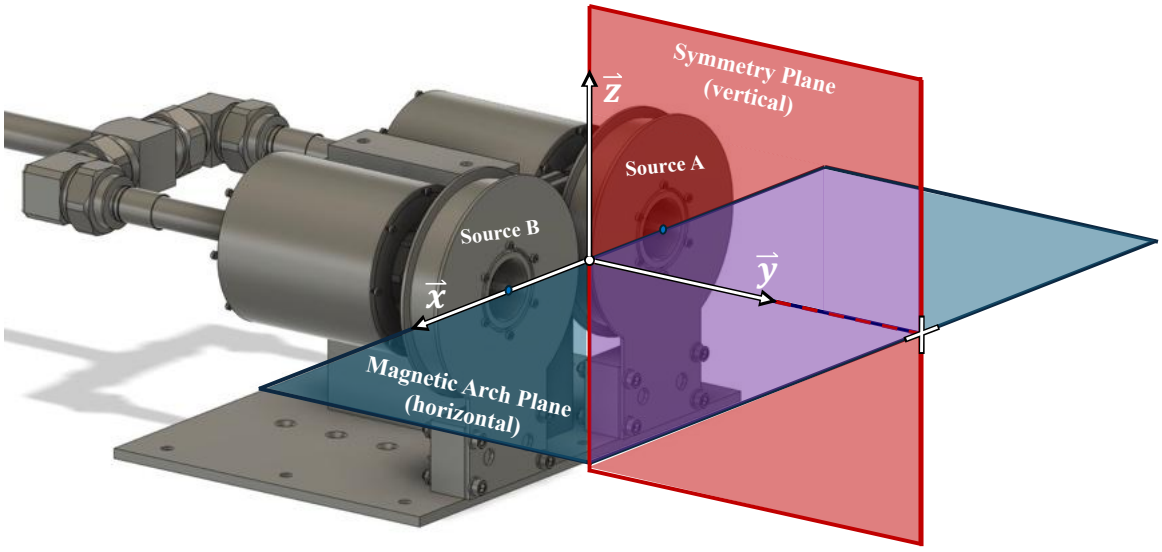

Figure 4.1: Measurement planes of the thruster: horizontal plane in blue, vertical plane in red.

4.1.2 Magnetic field topology

The field is measured as described in 3.2, and repeated for 3 conditions: first without the thruster in order the acquire the background signal of the Earth's magnetic field, then once with the coils turned off and once with a current of 2 A running in each coil. This allows to determine the field generated by the magnets and the coils respectively.

The results for the total magnetic field, i.e. permanent magnets and coils turned on with 2 A in each one, with the coil-generated field oriented with the permanent magnets are reported. This is the sole configuration of the magnetic field used during plume characterization experiments.

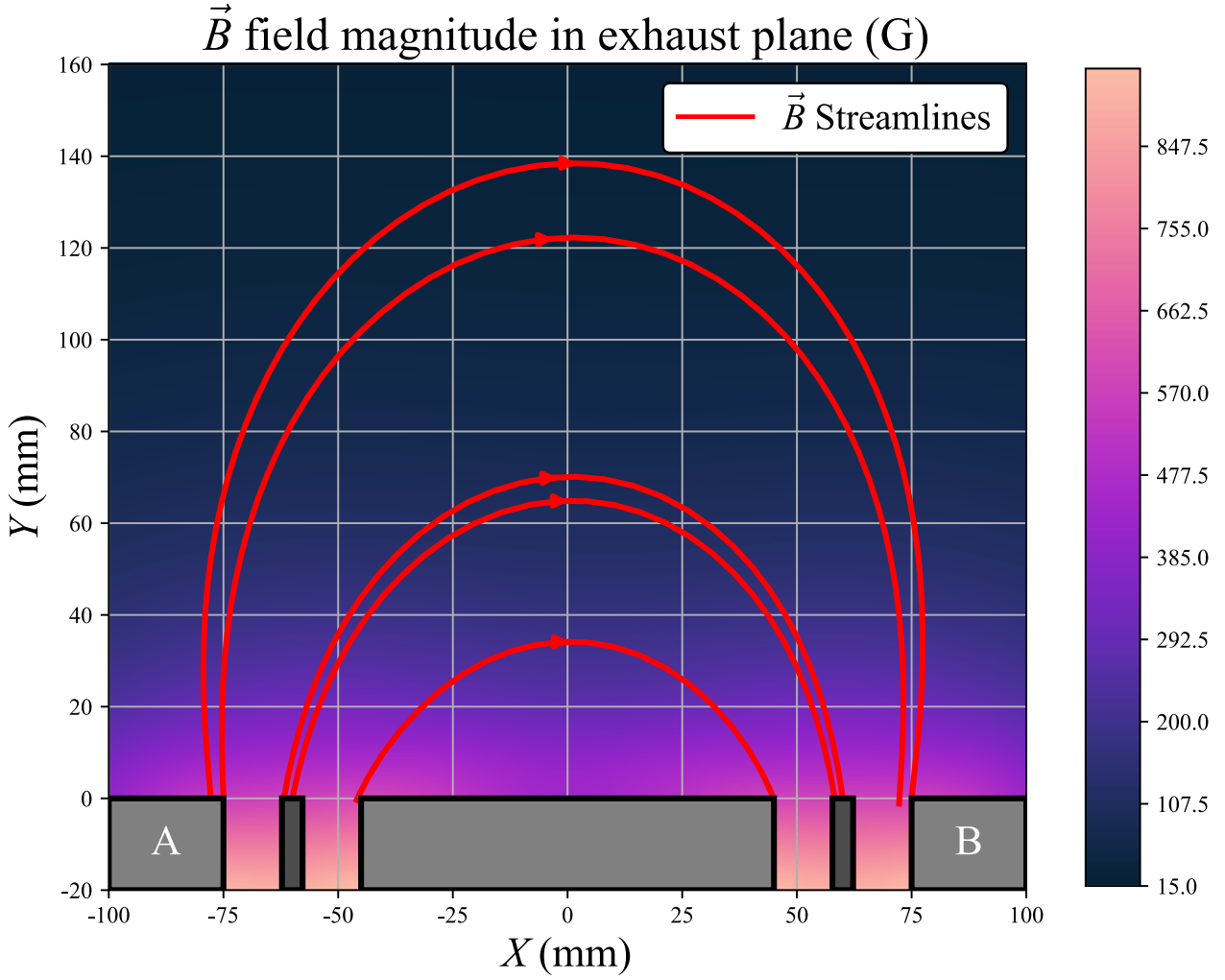

Figure 4.2: Magnetic field in the plume region (horizontal plane).

The results for the magnetic field presented in this section have been interpolated to obtain a continuous field approximation, using gaussian radial based functions interpolation.
The field in the region of the magnetic arch connecting the two sources is presented on fig.4.2, in the horizontal (exhaust) plane projection. The sources are labeled and characteristic streamlines are indicated by red lines. It is to be noted that there is a slight mismatch between the streamlines originating from each source (bottom right, on the outer side of source B), as the field is not perfectly symmetrical. This is likely due to an imperfection in the magnets inducing a field imbalance. The most outward streamline reaches its apex at 140 mm from the origin of the thruster, the most inward streamline reaches hers at 35 mm from the origin, those values are relevant for the choice of the location of plasma diagnostics measurement points as the focus is set on the arch which is expected to be denser in this location.
Along the magnetic streamlines displayed in red, the field presents a magnetic mirror configuration. Since the electrons are expected to be magnetized, this can lead to electrons being trapped in the magnetic arch and bouncing back and forth between sources.

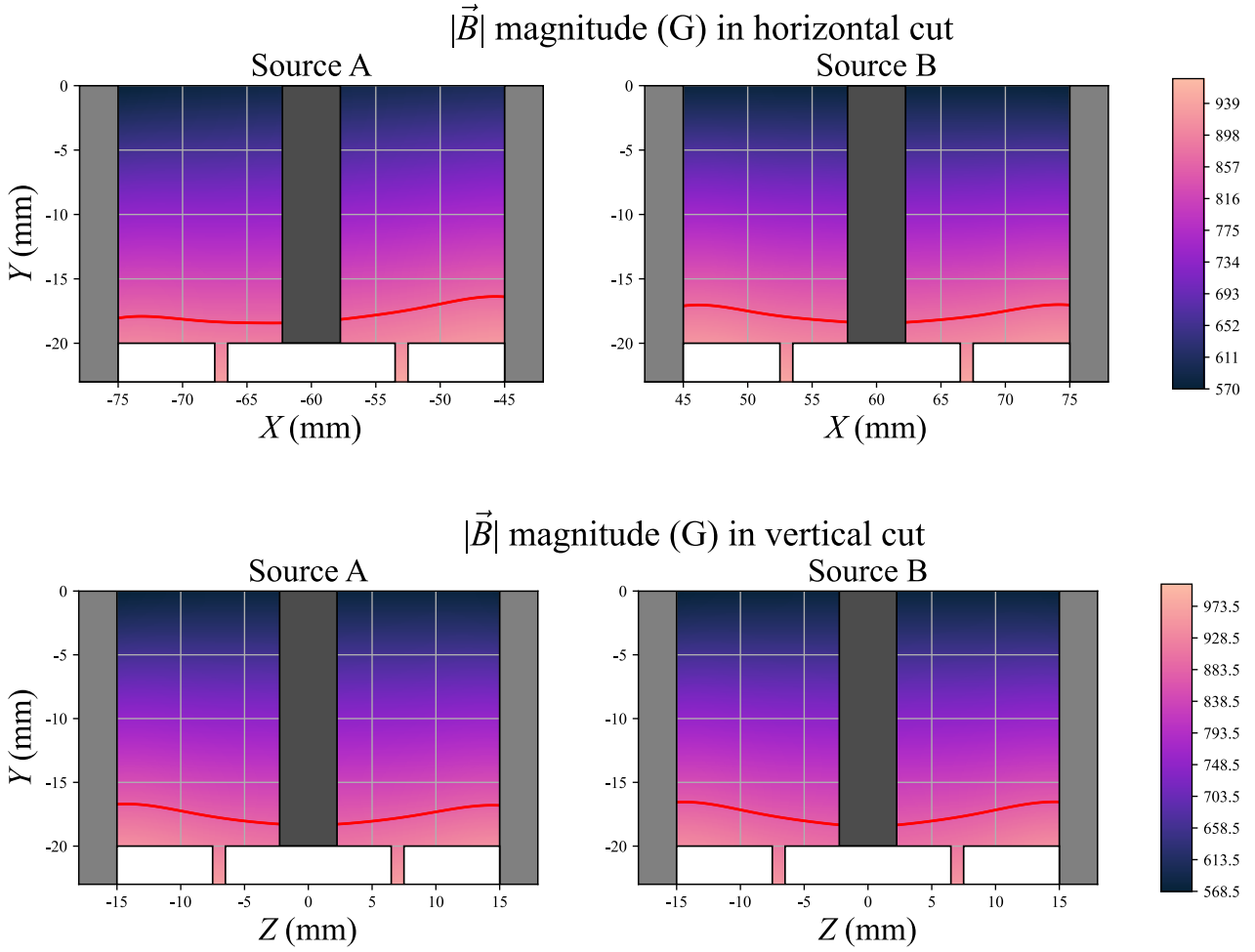

Figure 4.3: Magnetic field inside the plasma chambers along the horizontal plane (top) and vertical plane (bottom). The ECR region is indicated by the red line, plasma chamber walls (gray), antenna (dark gray), ceramics (white).

Another zone of interest for the magnetic field is the region located inside the plasma chambers themselves, as this is where the ionization occurs due to the ECR phenomenon which depends on the magnetic field intensity. The magnetic field strength in each source is presented in fig.4.3, both along the vertical and horizontal planes for comparison.
For the magnetic arch configuration used in this work (permanent magnets and 2 A in each coil), the ECR region (at 875 G) is relatively thin and sits deep inside the chambers, close to the gas injection (from the annular gap between the two circular ceramic pieces). Note the ECR region asymmetry between the two sources in the horizontal plane, where Source A shows an ECR region located further downstream on its right side, which is probably due to magnet defect. Although minimal, this asymmetry can be a cause for increased losses at the wall and reduced ion energy as ions generated further downstream should experience a smaller potential drop and thus a lower acceleration.

4.2 Far-plume measurements

4.2.1 Faraday cup measurements

The ion current density is measured by the Faraday cup in the far plume region at different operating points of the thruster. The forwarded (i.e. setpoint) microwave power P is varied between 50 W and 100 W, while the total mass flow rate (distributed to both sources via the common feed line) is set from 5 to 20 sccm of Xenon.

The results for the ion current density obtained in the horizontal plane are presented on fig.4.4. The first evident trend to be observed is the increase in current density with the mass flow rate, at all power settings, $P = 50$, 100, 150 W. As more neutrals are injected inside the plasma chamber, more ions are produced and accelerated downstream leading to the increase in current density. This is strongly non linear with mass flow rate, the ion current difference between 5 and 10 sccm is much greater than between 15 and 20 sccm. At the angle of peak current ($\theta = 48°$) for $P = 100$ W, moving from 5 sccm to 10 sccm yields a current difference of 136%, while going from 15 to 20 sccm only yields an 11% increase. The larger the microwave power, the higher the relative difference. This suggests that, for a given microwave power, the plasma chambers lose ionizing efficiency as larger mass flow rates are used, or that a large portion of the injected gas leaves the chamber while remaining neutral.
The other main trend is the current density increase with the microwave power, which is expected as larger forwarded power leads to more ionization and thus a larger current.
About the angular distribution of the current density, the curves show two peaks around $\theta = \pm 45°$, corresponding to the two sources. Those peaks tend to be more significant as the power is increased and at and above 5 sccm of mass flow rate. The center of the plume shows a lower current density than the sides, which can be described as a "hollow plume". This current distribution has appeared in the plume divergence of a single source waveguide ECRT in previous works [36]. However, in this case, it does not seem likely that each source presents a hollow profile but rather the cluster of two sources itself.
One operating point is qualitatively distinct from the others, at a mass flow rate of 5 sccm, the center of the plume is not as hollow as at other mass flow rate and presents a third peak, comparable in intensity to those at $\theta = \pm 45°$. At high power, $P = 150$ W, the central peak even shows the highest intensity out of the three. This may suggest a change in the regime of the thruster at low mass flow rate and high power or could be due to effects induced by the magnetic arch configuration.
Lastly, the current density profile presents a light asymmetry in terms of intensity of the peaks at $\theta = \pm 45°$, the peak on the right, corresponding to Source B, shows a slightly higher intensity, probably due to the magnetic field imbalance between the two sources, yielding a slightly less effective Source A.

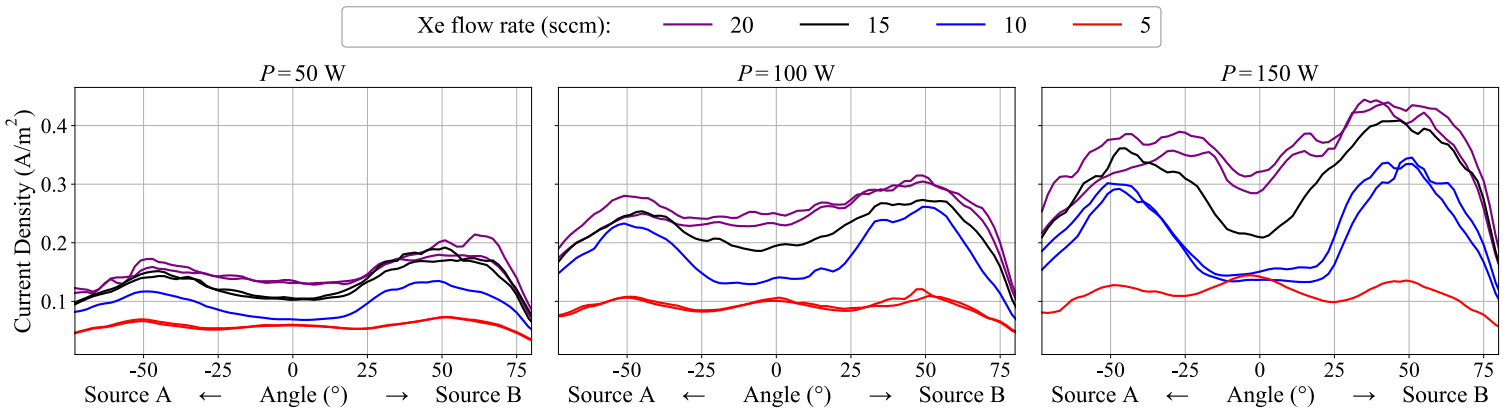

Figure 4.4: Faraday Cup measurements in the exhaust plane (horizontal).

In order to investigate the visually observed asymmetry in the plume exhaust (plasma beam escaping from the arch in the vertical direction), an ion current density scan is realized in the vertical plane between the two sources, the results are presented in fig.4.5. The same operating points as for the horizontal scan (fig.4.4) have been measured with the exception of 20 sccm mass flow rate.

The ion current density profile is coherent with the visual observations, a net asymmetry is observed on the curve with the current density being higher towards the top of the thruster, where the plasma beam is visually observed. The same trends with power and mass flow rate as in the horizontal plane can be observed, current density increases with mass flow rate and power.

A comparable hollowness to the one occurring in the horizontal plane can be observed, with the presence of a dent in the current density around $\theta = 20°$.

Another identical measurement is reproduced with the polarity of the magnetic arch reversed, the results are shown in fig.4.6. The orientation of the field definitely plays a role in the observed asymmetry, with the current density profile being reversed (higher current density towards the bottom) when the magnetic field is flipped. Note has to be taken that for the measurement with the magnetic field flipped on fig.4.6, the coils were wired improperly i.e. with non symmetric polarity between source A and B. The results can only be interpreted qualitatively to confirm the dependency of the plasma beam on the magnetic field direction but cannot be used to compare numerical values of the ion current density.

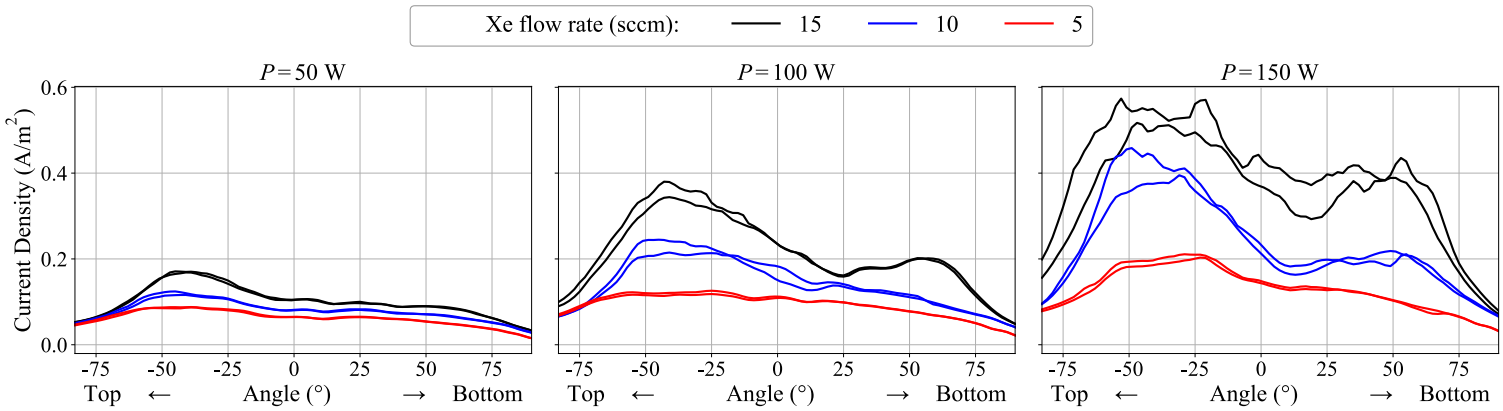

Figure 4.5: Faraday Cup measurements in the symmetry plane (vertical).

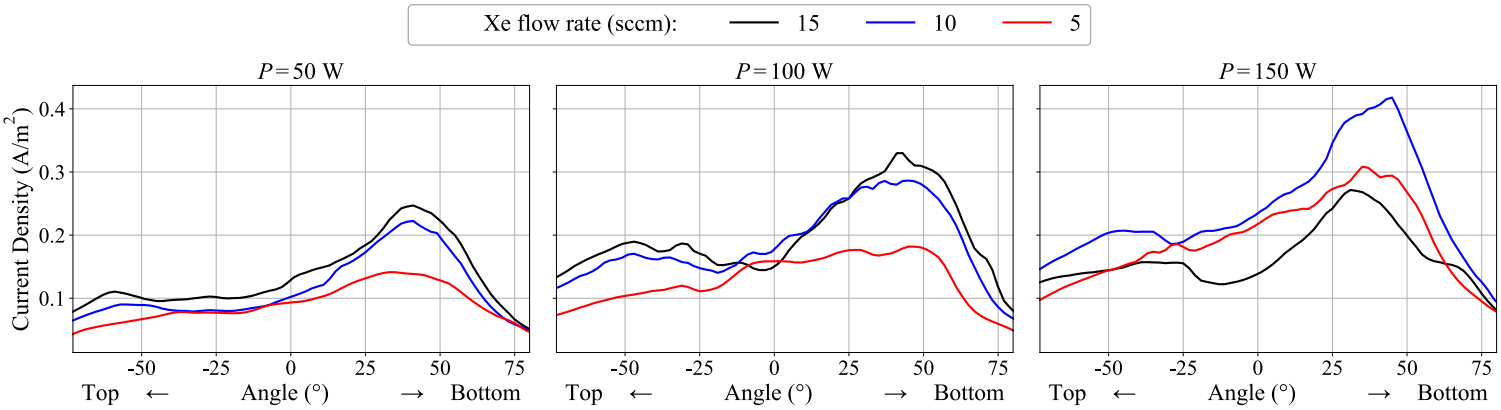

Figure 4.6: Faraday Cup measurements in the symmetry plane (vertical) magnetic field is reversed.

4.2.2 Retarded potential analyzer measurements

Based on the results obtained through Faraday cup measurements, the IEDF has been measured with the RPA at the same operating points and at two different angles in the horizontal and vertical plane.
In the horizontal plans, the angles chosen are the center line ($\theta = 0°$) and the location of the highest peak ($\theta = 42°$ or $\theta = 48°$, depending on the power setting), the results are presented in fig.4.7.
One common feature of the IEDF at both angles is the the relationship between mass flow rate and ion most probable energy, referred from there as ion energy. The ion energy increases as the mass flow rate decreases, whereas the energy peak intensity decreases (coherent with FC measurements and lower ion population at lower mass flow rate). This trend is observed at all power settings and at both angles, indicating an overall stronger acceleration of the ions downstream at lower mass flow rates.
Comparing the IEDFs at the centerline ($\theta = 0°$) and at the peak current density angle ($\theta = 42°$ on the Source B side), one observes that the distribution functions are systematically more peaked and centered around the maximum at the higher angle, while the ion energy is relatively unchanged. This broader ion energy distribution in the center of the magnetic arch could suggest that specific acceleration mechanisms are occurring inside the arch only, and that those mechanisms both accelerate and slow certain ions down, thus the broader distribution.
Another noticeable difference between the IEDF at the two angles is the presence of a low energy ion population that is more pronounced on the centerline, at the center of the arch. A possible explanation could be that a secondary population of ions is generated inside the magnetic arch, through ionization of neutrals by the electrons circulating inside the arch. This population would then be accelerated downstream and acquire a lower velocity than the primary population which is generated inside the plasma chambers.
The impact of microwave power on the IEDF is relatively limited with a marginal increase in ion energy with the power. The overall peak intensity still increases with power, which is coherent with the FC measurement, since a higher power setting implies a larger number of ions produced.

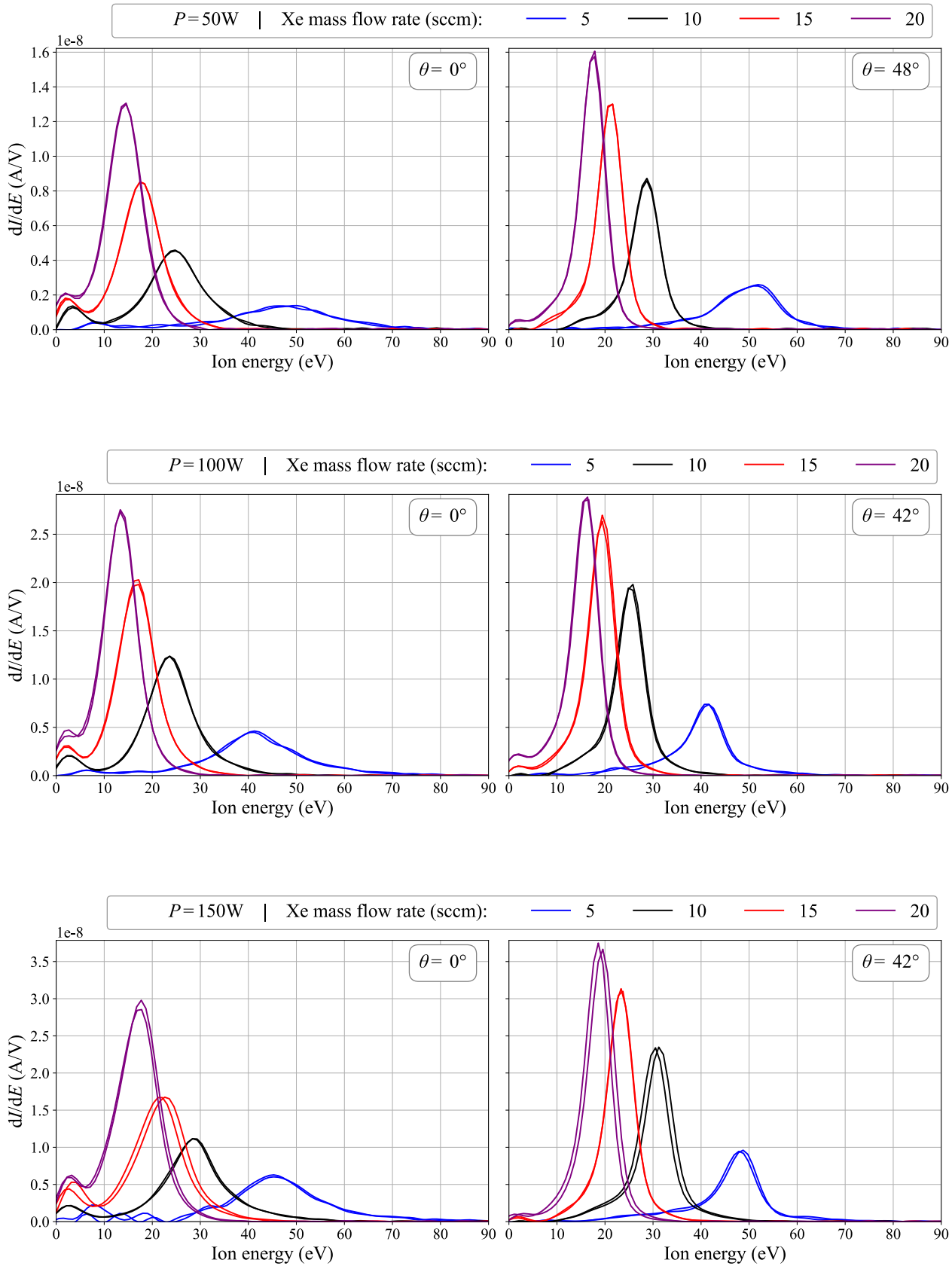

Figure 4.7: IEDF along the centerline and the peak ion current angle, at different operating points, in the horizontal plane.

The results of the RPA measurements in the vertical plane are shown on fig.4.8, in a similar way to the horizontal plane: IEDF along the centerline and the angle of maximum current density $\theta = -33°$ (from the FC measurement).
Common trends with the vertical plane can be observed: as the mass flow rate increases, the peak intensity increases and the ion energy decreases. The same low energy secondary ion population is present. The IEDFs along the centerline ($\theta = 0°$) are in good agreement with the ones obtained for the horizontal plane on fig.4.7 along the same centerline (the centerline in both planes are the same). This similarity is indicative of the repeatability of the thruster. The differences can be explained by minor modifications of the alignment of the thruster pieces and of the microwave transmission lines, as the thruster had to be disassembled in between the horizontal and vertical plane measurements.
Comparing the IEDFs between the two angles provides information on the asymmetry observed in the plasma beam. Along the maximum current angle, the peak intensity is higher, implying that the majority of the ions are ejected outside of the horizontal exhaust plane (at least in the vertical plane), the ion energy is however almost the same for both angles. It could have been valuable to also perform vertical scans right in front of each source in addition to the central plane measurement.
An interesting feature is the double peak of the ion energy for 150 W and 5 sccm at ($\theta = -33°$), almost no low energy ion population can be seen, but two distinct peaks around 40 and 55 eV are observed. A similar yet less distinct behavior can be seen at 100 W as well. It seems that in the vertical plane and at low mass flow rate, ions are ejected out of the magnetic arch with a non-Maxwellian energy distribution.
Going back to the aforementioned low energy ion population observed on both the horizontal and vertical plane, with stronger peaks along the centerline. One can observe that for 5 sccm of mass flow rate, this population is either absent or almost undistinguishable, reinforcing the hypothesis that the plasma sources have a higher ionization rate at low mass flow. Less neutrals escaping the chambers without being ionized lead to fewer secondary ionization in the arch explaining the observations on fig.4.7 and fig.4.8.

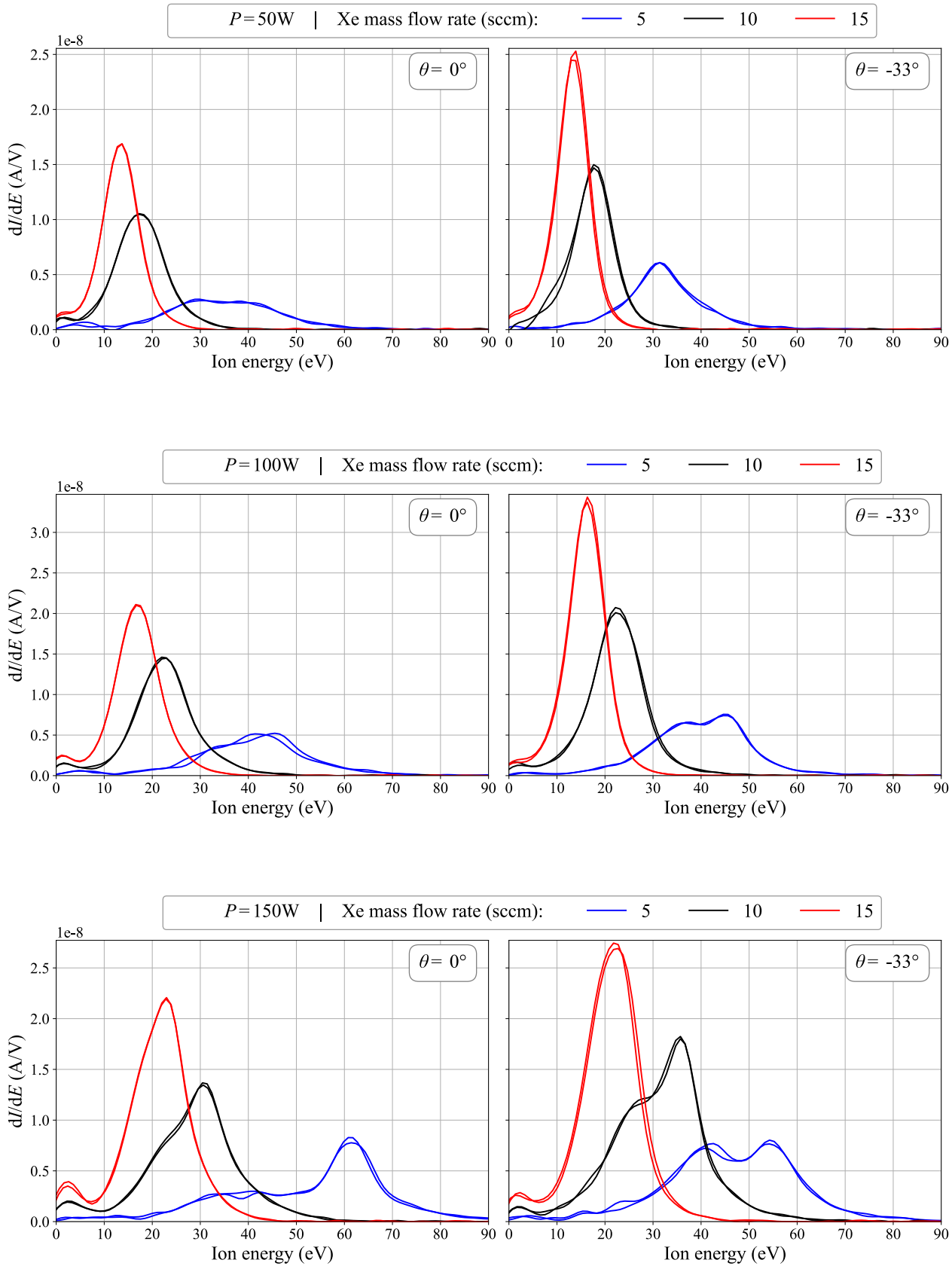

Figure 4.8: IEDF along the centerline and the peak ion current angle, at different operating points, in the vertical plane.

As mentioned previously, a second measurement was performed in the vertical plane with the polarity of the magnetic field reversed. Based on the FC measurement on fig.4.6, the IEDF is acquired along the centerline ($\theta = 0°$) and at the angle of maximum ion current density, ($\theta = 36°$) in this case. Even if only the power setting of 100 W was investigated, with improper wiring of the coils, the IEDF are presented in fig.4.10. The same split of the ion population as in the other vertical measurement can be seen, but with an increased gap in energy. It is difficult to conclude on this energy split or to link it with one observed in fig.4.8. One possible reason for the split is that one of the two coils was wired in such a way that its magnetic field was opposing the permanent magnet, leading to a reduced field in the chamber and worsening the ionization and acceleration performances. The lowest energy populations observed could then be originating from the source with improper wiring. This hypothesis fits the observation of a slightly lower peak intensity for the low energy population, supporting the inferior ionization in that source.

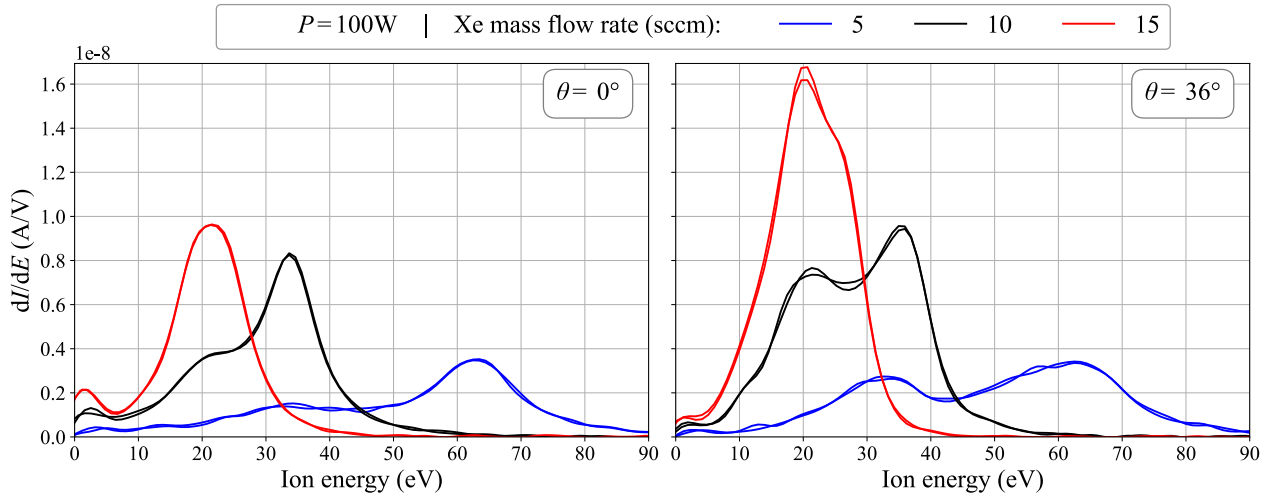

Figure 4.9: RPA measurements in the symmetry plane (vertical) at 100 W, the magnetic field is reversed.



Figure 4.10: Photograph of the exhaust plasma plume for $P = 100W$, mass flow rate of 15 sccm (left) and 5 sccm (right).

4.3 Langmuir probe measurements in the horizontal plane

4.3.1 Full plane characterization

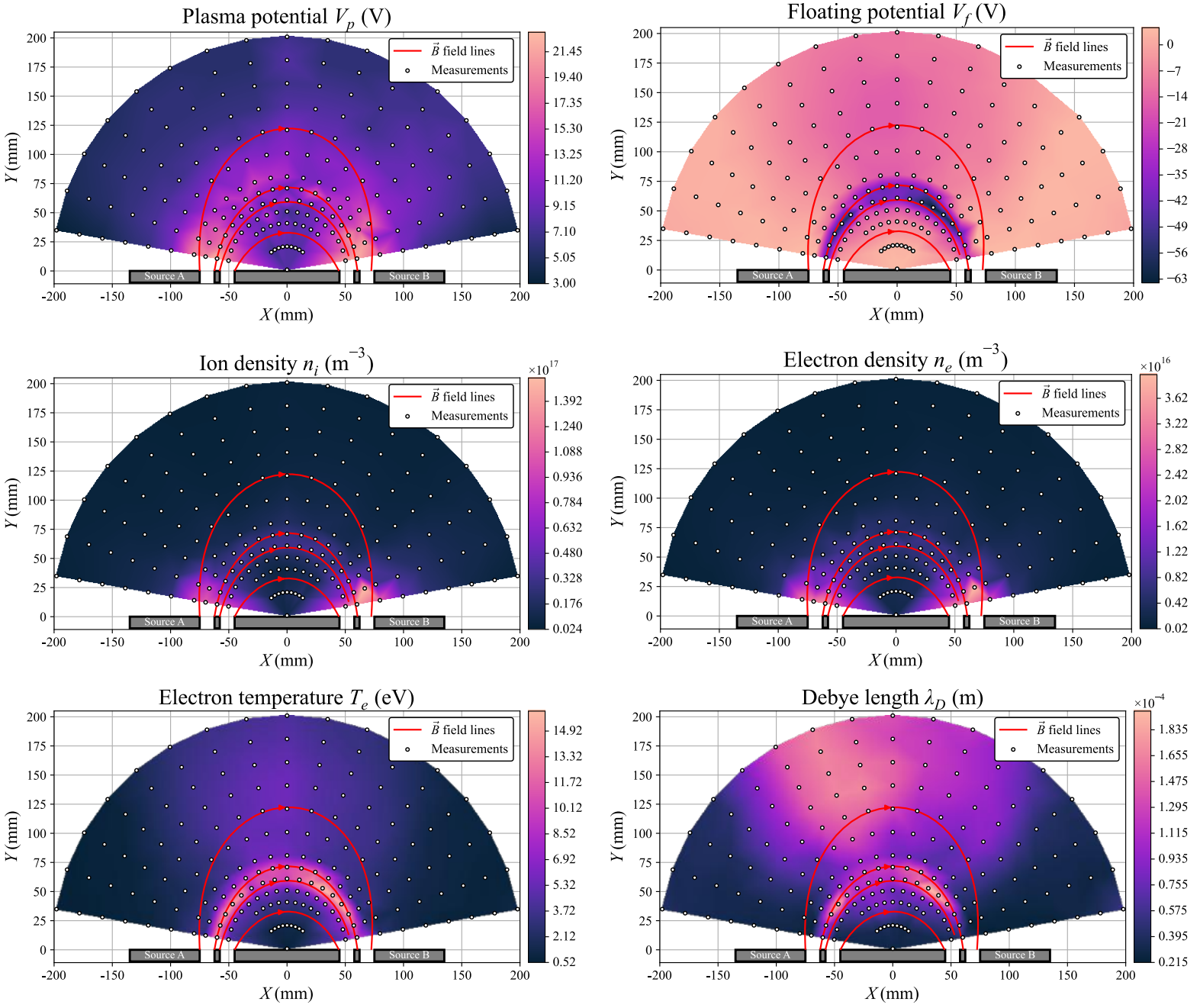

Figure 4.11: Plasma parameters in the horizontal plane at 100 W, 10 sccm Xe.

A full plane characterization of the exhaust plume was performed using Langmuir probes. Based on the FC and RPA measurements in fig.4.4 and fig.4.7 respectively, the operating point at a power of 100 W and 10 sccm of mass flow rate was selected.
This point represents a compromise between high enough ion energy and sufficient ion current

to facilitate the measurement using Langmuir probes. On a thermal point of view, selecting a power setting of 100 W instead of 150 W has a significant impact on the heating rate of the thruster, allowing for more measurements during a continuous period of operation. The reduction in ion current density at 10 sccm compared to 15 sccm is marginal as one can see on fig.4.4.
Langmuir probe measurements are acquired on a semi-circular grid spanning $\theta = \pm 80°$ from the thruster's y axis. Care was taken to densify the measurement grid in the magnetic arch region. The results are presented as colormaps and the exact locations of measurements are indicated by dots in the figures. The sources walls and antennas are represented by gray rectangles, sources are labeled. The magnetic streamlines originating from the sources and antennas edges are indicated by red lines.

About the plasma potential V_p, its value is highest close to the exhaust of the chambers, with values in the vicinity of 22 V. Those potential values are coherent with the ion energies measured with the RPA (see fig.4.7) which shows an ion energy peak at approximately 24 eV for 100 W and 10 sccm. The difference between the RPA measured peak energy (24 eV) and the plasma potential (22 V) could be explained by the fact that inside the chambers, which are inaccessible to the Langmuir probe, the plasma potential is likely slightly higher than 22 V.
Data shows a slightly higher potential at the exhaust of source B, which could confirm the hypothesis on source efficiency due to magnetic field imbalance. However, the potential difference between the sources is low and falls inside the margins of error, preventing any definitive conclusion. One can notice that the magnetic arch region is marked by high plasma potential values, noticeably around the streamlines originating from the antennas.
The floating potential is relatively uniform with the arch region displaying large negative values down to -63 V. Similarly to the plasma potential, the magnetic tube originating from the antennas contains the most negative values. This behavior is even more pronounced than for V_p.
The electron temperature T_e follows the behavior of the floating potential, with a population of hot electrons confined in the arch, around the streamlines originating from the antenna. The temperature reaches up to 15 eV, with maximums located around 50 mm downstream of the sources, on the antenna streamlines. The presence of hot electrons, above 12.13 eV (first ionization energy of Xenon) in the arch region supports the hypothesis on secondary ionization inside the arch formulated in 4.2.1. The fact that the hottest electrons are closest to the streamlines originating from the antenna suggests that electrons are heated with more efficiency close to the antenna. This is likely due to the larger intensity of the microwave electric field close to the antenna [43]. Downstream of the magnetic arch, a conical region of cooler electrons (around 7 eV, still hotter than the background) can be seen expanding from the arch. This suggests that a portion of the electrons escapes the arch and detaches from the streamlines.
About the electrons and ions densities, their values are in the order of 10^{16} to 10^{17} respectively. This discrepancy between the two species is due to the assumptions in the model used to post process the Langmuir probe data and do not necessarily reflect violation of quasi neutrality of the plasma. The value for electron density is the one that should be considered as the most accurate. On the distribution of the densities, they are very similar as the plasma is quasi neutral and with maximums located closest to the exhaust of the sources, as expected. The arch region naturally presents a lower density than the exhausts, with the plasma being largely denser close to the antenna streamlines. The outer sections of the arch where the streamlines originate from the chambers edges are more depleted.

4.3.2 Gas flow rate effects

Analogous to the measures performed with the FC and RPA in 4.2.1, a scan of the plume with Langmuir probes is performed at two mass flow rates: 5 and 15 sccm. The measurement mesh chosen sparser than for the full scan and is limited to the plume region on side of the source B, as it is the one displaying the strongest magnetic field.
Measurements are performed at a radius $r \in \{50, 70, 120, 200\}$ mm from the thruster's origin, for angles comprised between 0 and 80° with steps of 10 °. Results are displayed on fig.4.12 for 5 sccm and fig.4.13 for 15 sccm.
Coherently with the RPA measurements, the plasma generated with a mass flow rate of 5 sccm (fig.4.12) displays greater plasma potential, a lower floating potential and hotter electrons than at 15 sccm (fig.4.13). The electron and ion densities are approximately half of the values measured at 15 scmm, which is consistent with the lower amount of Xenon injected. The spatial distribution of the densities almost does not vary qualitatively from the nominal case at 10 sccm. One can only note that at 5 sccm, the density value drops quicker downstream of the chamber than at 15 sccm.
There is a dramatic decrease in electron temperature with mass flow rate, the maximum temperature drops from 20 eV at 5 sccm, to around 5 eV at 15 sccm. The distribution of temperature is also influenced, it is more uniform at 15 sccm whereas at 5 sccm, the core of the arch is noticeably hotter than the rest of the plume. This suggests that lower densities are associated with better and more localized power absorption by the plasma. In fact at higher mass flow rates, thus higher densities, there are likely more inelastic collisions causing T_e to decrease overall and become more homogeneous, since the electrons thermalize via collisions.
Similarly to the electron temperature, the plasma potential is also greatly reduced at 15 sccm. The difference between the peak plasma potential and the background potential downstream of the thruster increases as the mass flow rate decreases, confirming that acceleration becomes more efficient at a lower mass flow rate.

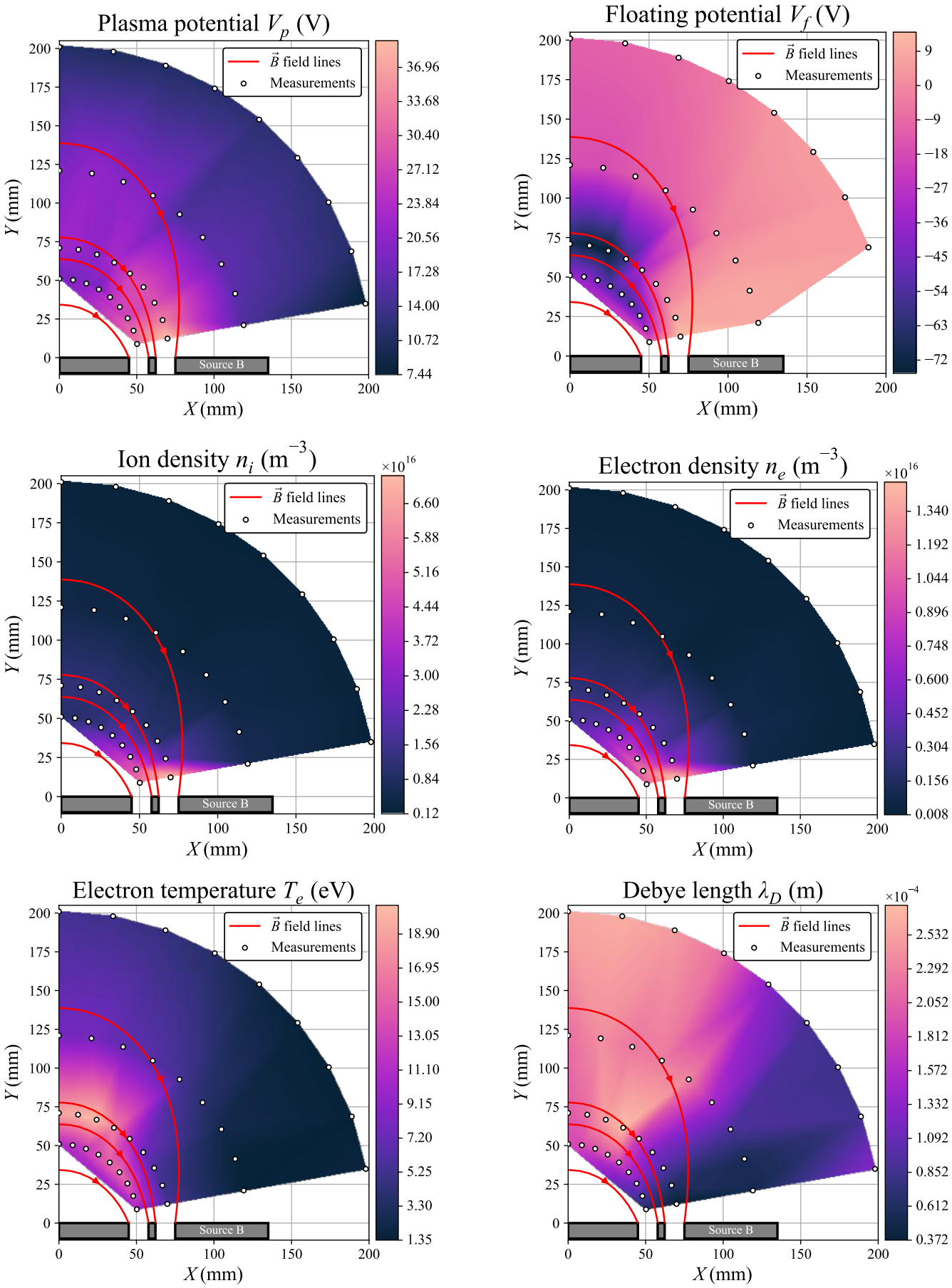

Figure 4.12: Plasma parameters in the horizontal plane at 100 W, 5 sccm Xe.

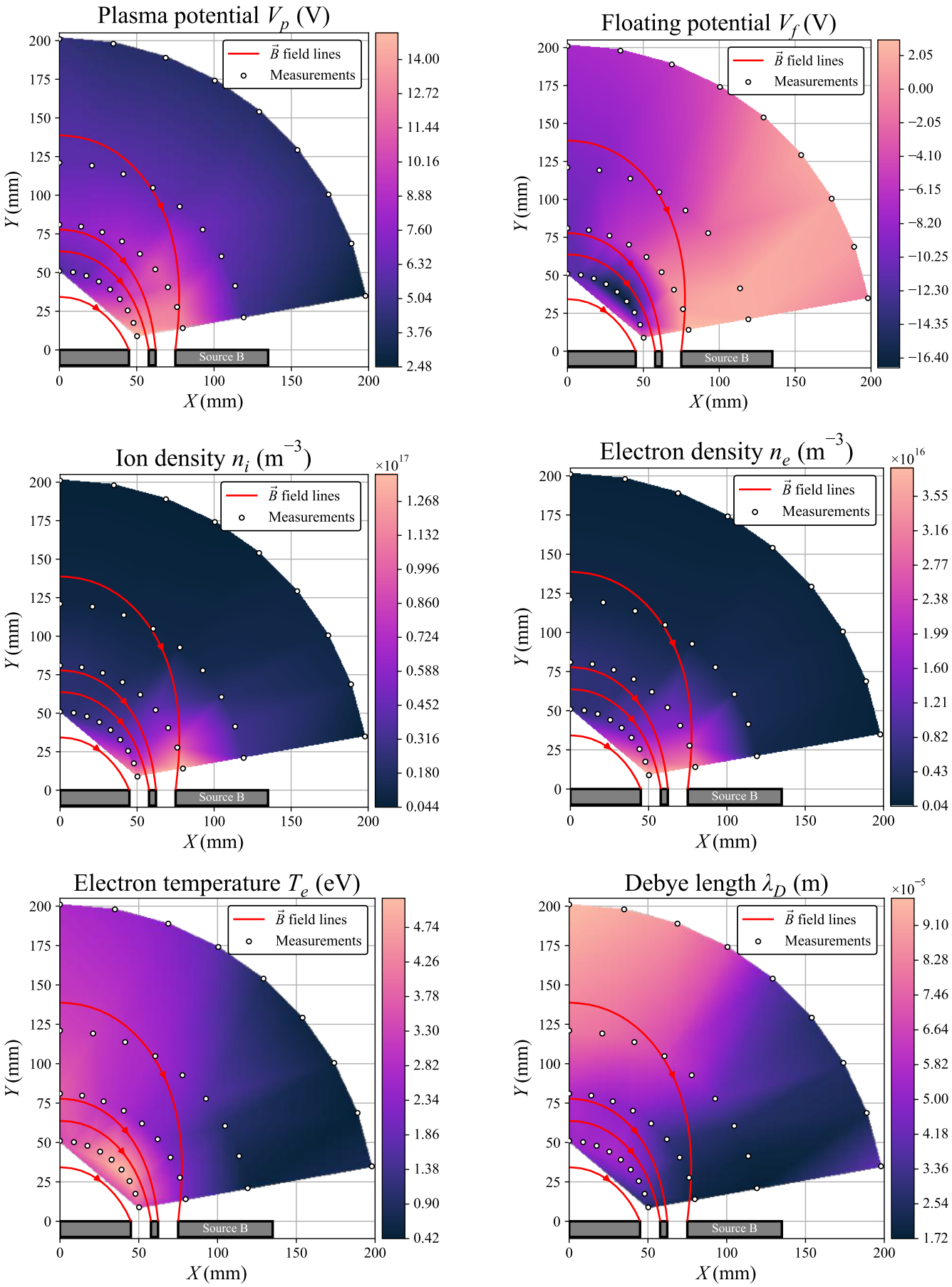

Figure 4.13: Plasma parameters in the horizontal plane at 100 W, 15 sccm Xe.

4.4 Langmuir probe measurements in the vertical plane

4.4.1 Full plane characterization

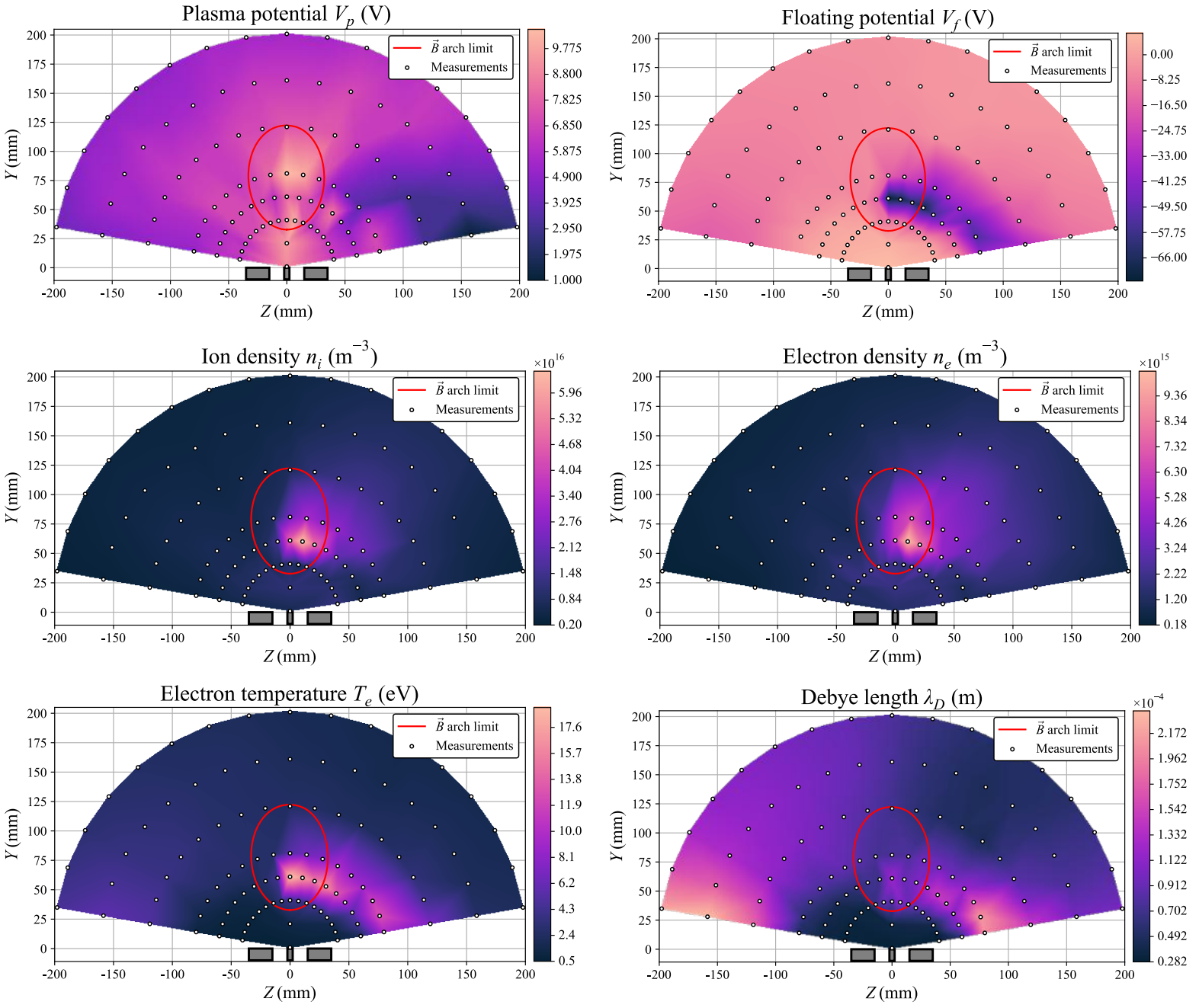

Figure 4.14: Plasma parameters in the vertical plane at 100 W, 10 sccm Xe.

Similarly to the measurements performed in the horizontal plane in 4.3.1, a full characterization of the vertical plane is performed. The selected mesh is slightly coarser than for the horizontal plane. The results are presented as colormaps, location of measurement points are indicated by dots on the figures. The intersection of the magnetic tube (formed by the outermost streamlines

originating from the sources edges) with the vertical plane is indicated by a red line.
The first interesting observation is the relative uniformity of the plasma potential, one could expect the value to drop rapidly as the angle diverges from 0° but the distribution of V_p is relatively conical with a weak gradient. The other main observation is the asymmetric behavior of the plasma in the vertical plane, as previously revealed by the FC and RPA measurements. There is a notable shift towards the top of the thruster.
The floating potential is displaying its most negative value in the magnetic arch, as expected and in coherence with the horizontal plane measurements. However, a region of largely negative potential is seen on the top of the magnetic arch and expands in a curved way. The same is observed for the electron temperature. About the electron and ion densities, a comparable shift is observed, without the curved shape but with a marked asymmetric expansion towards the top. Discussions on the possible reasons for this asymmetry are presented in 4.5.

4.4.2 Gas flow rate effects

As it was done in the horizontal plane, measurements were taken in the vertical plane at 5 and 15 sccm. Contrary to the horizontal plane, a full scan is performed due to the strongly asymmetric behavior of the plasma in the vertical plane. To reduce the number of measurements, the mesh density is reduced compared to the full scan, with less points on the "empty" side, i.e. for negative values of Z. Measurements are performed at a radius $r \in \{50, 70, 120, 200\}$ mm from the thruster's central point, for angles comprised between 0 and 80° with steps of 10° on the "dense" side and 20 ° on the "empty" side. Results are displayed on fig.4.15 for 5 sccm and fig.4.16 for 15 sccm.

The first observation is that the asymmetry is more pronounced with a low mass flow rate of 5 sccm than with 15 sccm, noticeably for the electron and ion density as well as for the plasma potential. For the plasma potential specifically, it is strongly asymmetric at 5 sccm and relatively homogeneous at 15 scmm. Comparably to he case at 10 sccm (fig.4.14) the plasma is strongly asymmetric, with hot electrons present clearly outside of the magnetic arch. The hottest ones are still at the center of the arch, but the top (positive Z) of the plane contains noticeably hotter electrons than the bottom.
About the plasma and floating potential values, the results are comparable to those obtained in the horizontal plane, the magnitude of the potentials is approximately reduced by half when moving from 5 to 15 sccm of mass flow rate. The electron temperature is also halved.
Comparing the densities between the two mass flow rates, a factor of approximately 3 is found between the densities at 5 and 15 sccm which is highly coherent with the mass flow rates. When looking at the spatial distribution of densities, the electrons and ions are more present on the positive side and confirm again that the plasma does not escape purely horizontally from the arch.

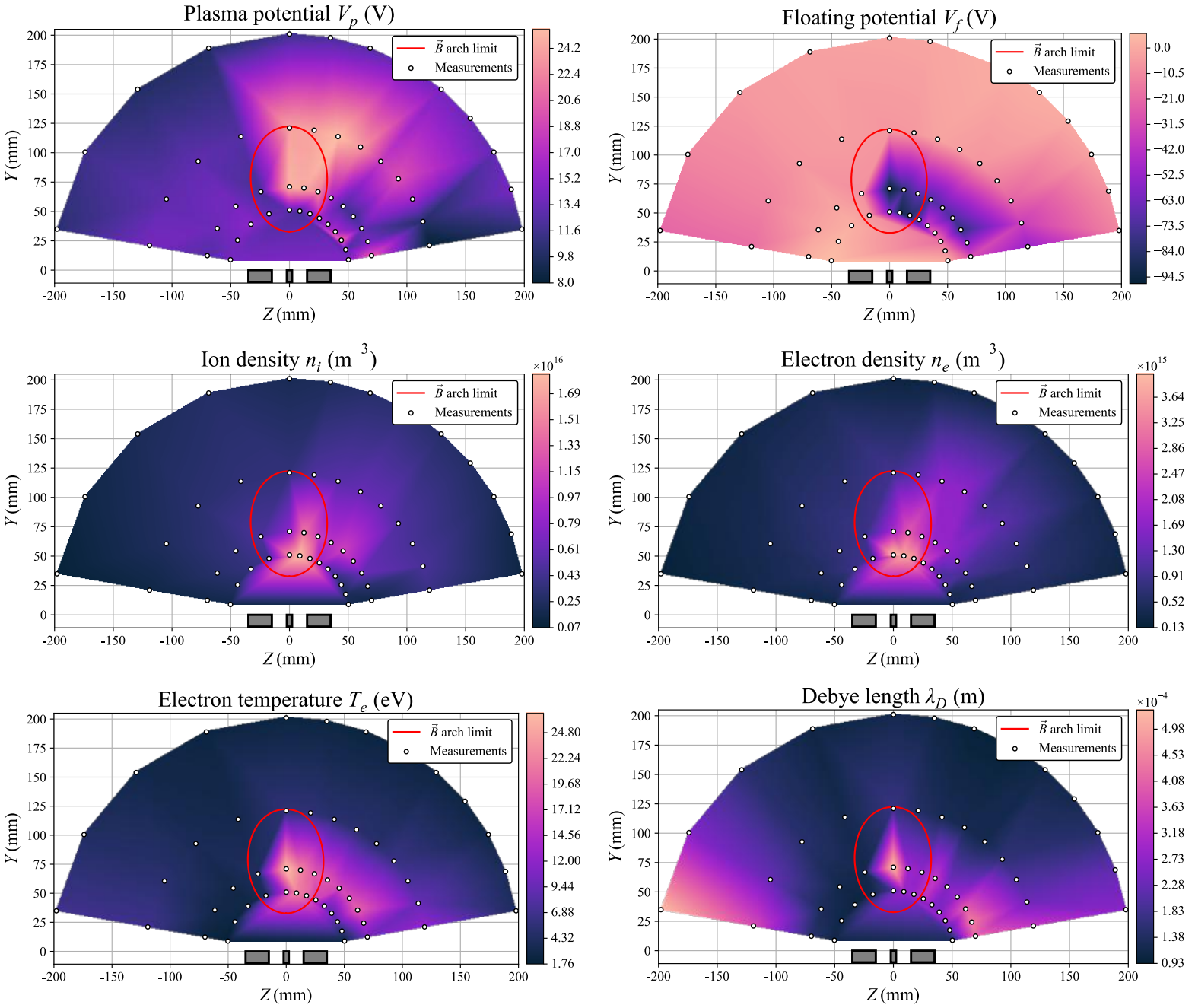

Figure 4.15: Plasma parameters in the vertical plane at 100 W, 5 sccm Xe.

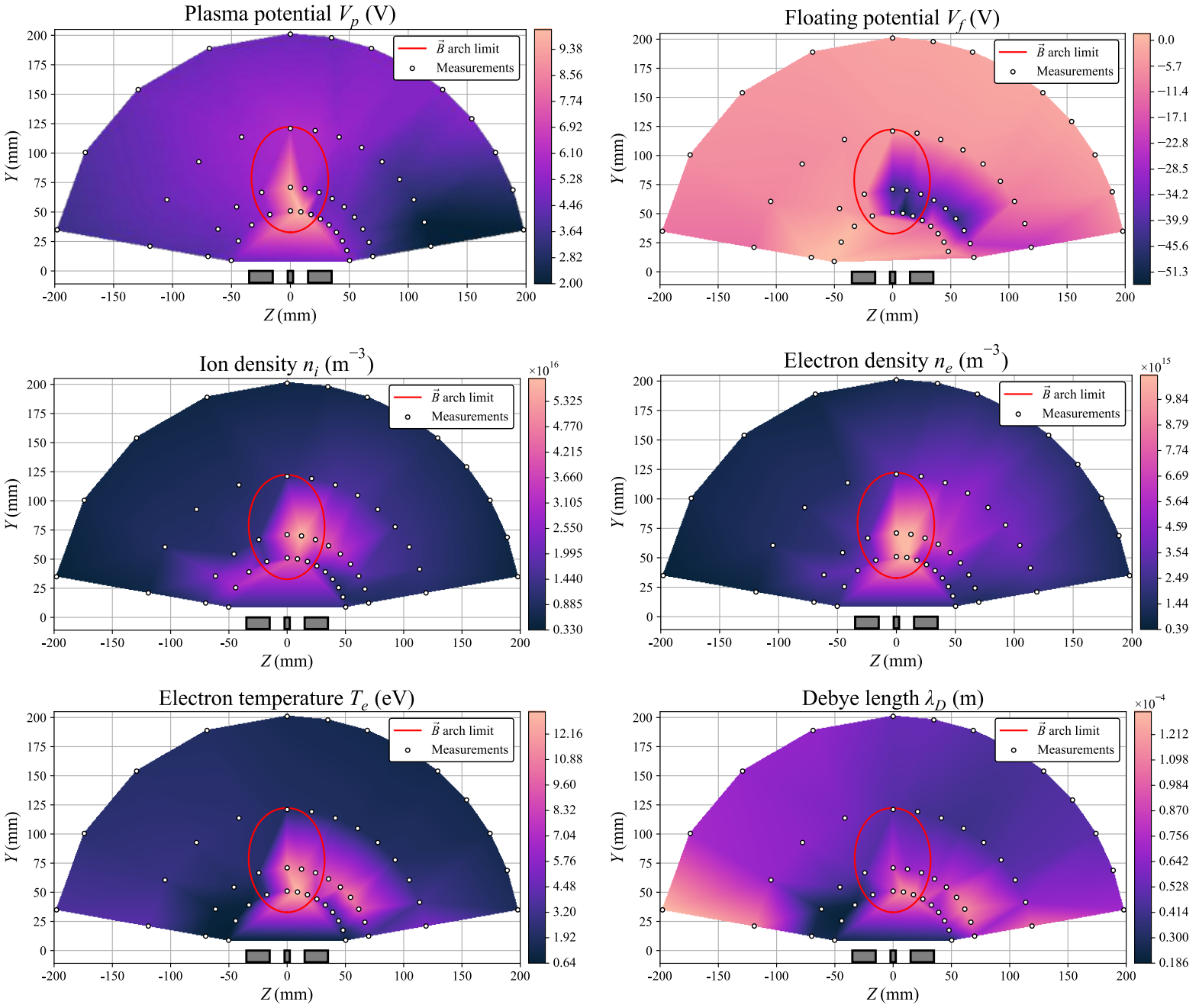

Figure 4.16: Plasma parameters in the vertical plane at 100 W, 15 sccm Xe.

4.5 Plasma asymmetries and $\vec{B}$ field induced drifts

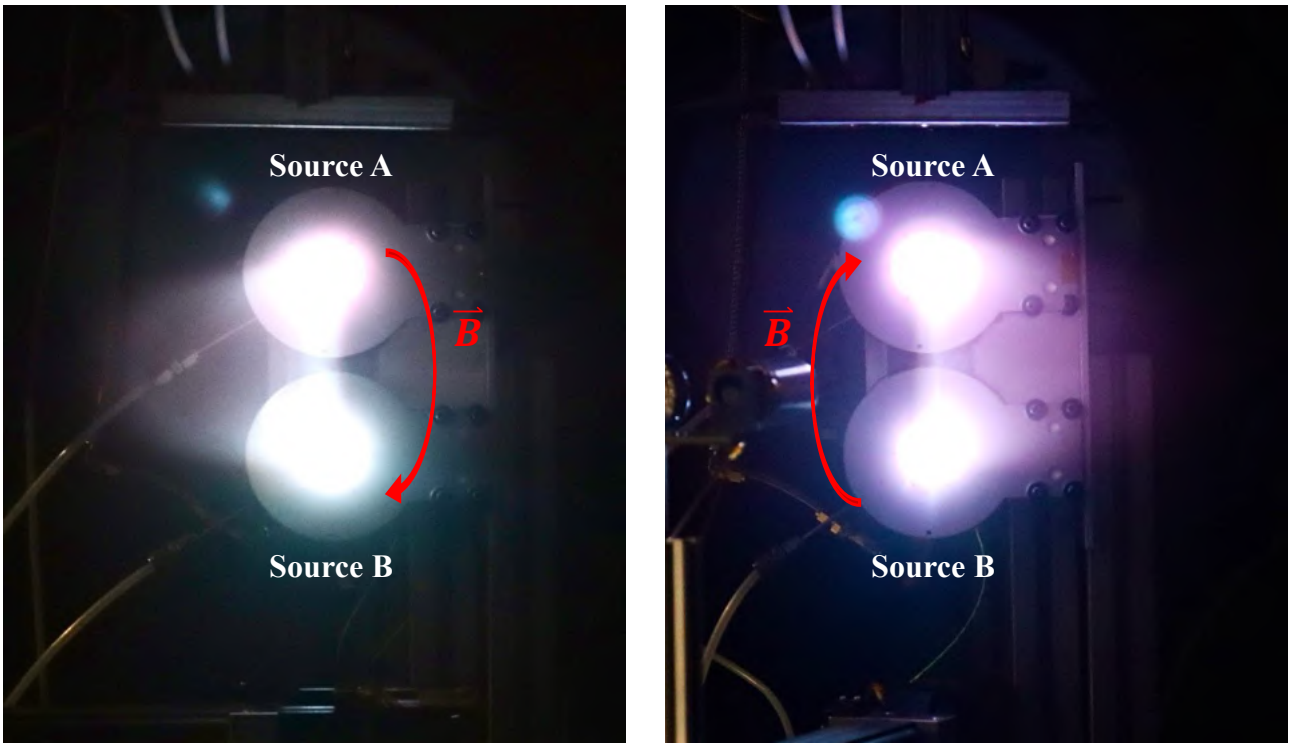

Figure 4.17: Photographs of the plasma plume from the front ($P = 100$W, 10 sccm), nominal magnetic field orientation (left) and reversed (right).

As one can see on the pictures in fig.4.17, the location of the plasma asymmetry (U-shaped plasma surface perpendicular to the magnetic arch) is dependent on the field orientation. When the field orientation is reversed, the asymmetry moves to the other side of the thruster. This dependence on the magnetic field orientation suggests that the asymmetry may be caused by drift phenomenons in the plasma, whose directions are dependent on the field's orientation.

4.5.1 Larmor radius

The Larmor radius of the electrons for the horizontal plane measurement at 100 W, 10 sccm is presented in fig.4.18. The velocity of the electrons is obtained from their temperature T_e assuming isotropic thermal speed distribution. This is however a strong assumption. In the ECR region itself, where most of the plasma is generated, the electron temperature should be anisotropic due to ECR heating in the perpendicular plane to the magnetic streamlines. The electron temperature measured inside the arch is probably disrupted by energetic fast electrons originating from the plasma source with high velocities parallel to the streamlines. Those hypothesis are however difficult to analyze experimentally.
The Larmor radius shows that inside the magnetic arch, the electrons essentially stay very magnetized and follow the streamlines with radius inferior to 3 mm. This indicates that the behavior of the electrons in the arch are mostly governed by magnetic field effects. Only the fast electrons generated inside the plasma chambers can escape the arch. The plasma Beta parameter (the ratio between plasma and magnetic pressure $\beta = 2\mu_0 n k_b T/B^2$) confirms this in fig.4.19. The magnetic effects largely dominate the electrons behavior.

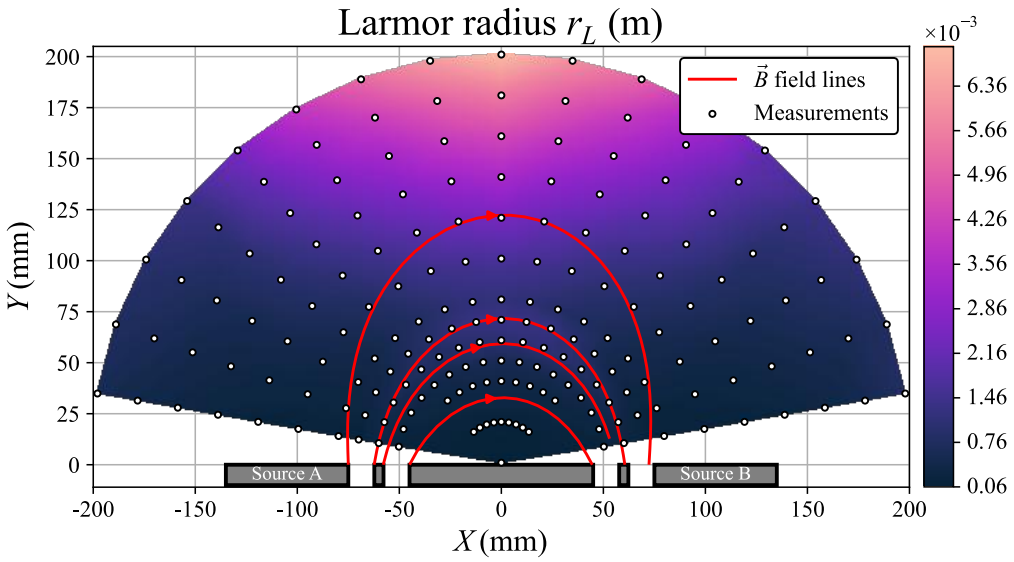

Figure 4.18: Larmor radius of the electrons in the horizontal plane.

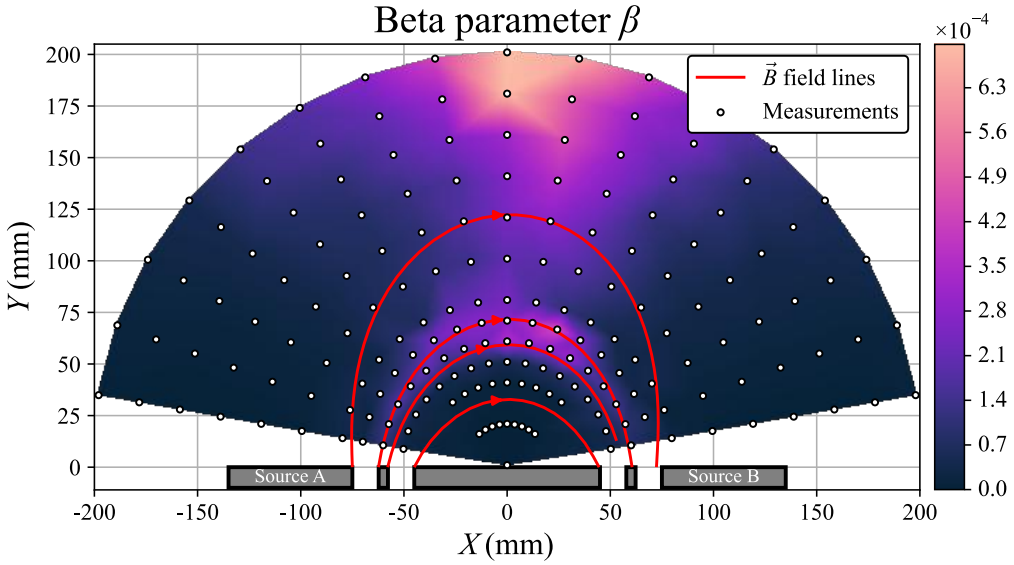

Figure 4.19: Beta parameter of the plasma in the horizontal plane.

4.5.2 $\vec{E} \times \vec{B}$ drift

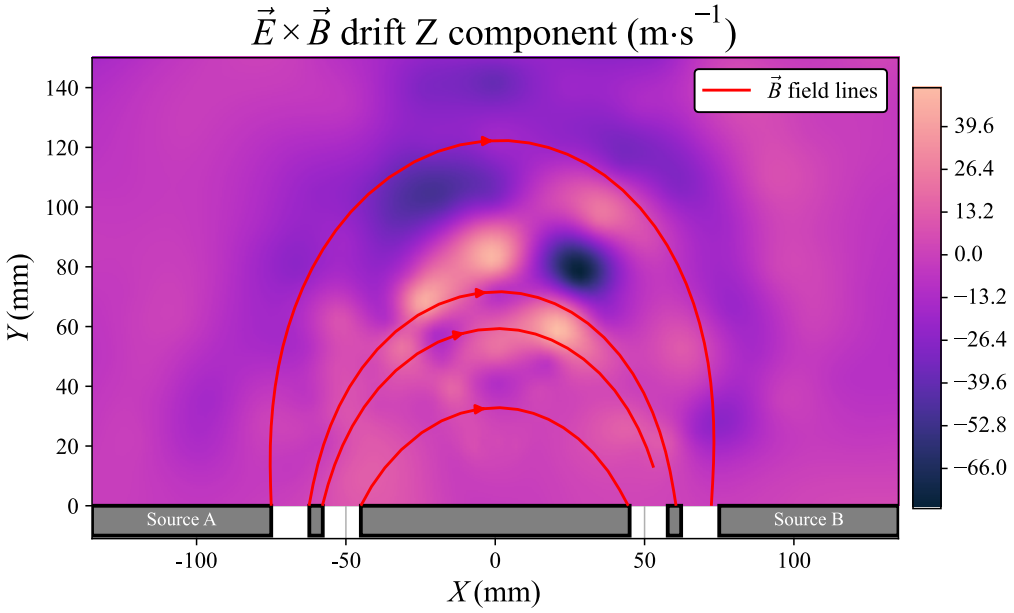

Figure 4.20: Vertical speed of the $\vec{E} \times \vec{B}$ drift.

The vertical component (along the Z axis, out of the plane of the figure) of the $\vec{E} \times \vec{B}$ drift velocity is displayed on fig.4.20. This data is obtained from the values of the plasma potential in the horizontal plane measurement at 100 W, 10 sccm (see fig.4.11). The electric field $\vec{E}$ is obtained by interpolating the plasma potential on the full domain using cubic splines then taking the gradient of the interpolated potential. Note that due to the V_p measurement not being smooth, the computed electric field and thus the $\vec{E} \times \vec{B}$ velocity map are relatively noisy. One can see that the region between the magnetic streamlines originating from the antennas is presenting positive values of drift velocities, which is coherent with the orientation of the asymmetry: for all measurements with Langmuir probes, the magnetic field was in the nominal configuration i.e. asymmetry towards the top of the thruster. The value of the drift velocity are however very low (tens of m·s^{-1}) compared to the in plane velocities of the plasma. The $\vec{E} \times \vec{B}$ drift is thus expected to contribute to the asymmetric behavior but is likely not its sole origin.

4.5.3 $\nabla\vec{B}$ drift

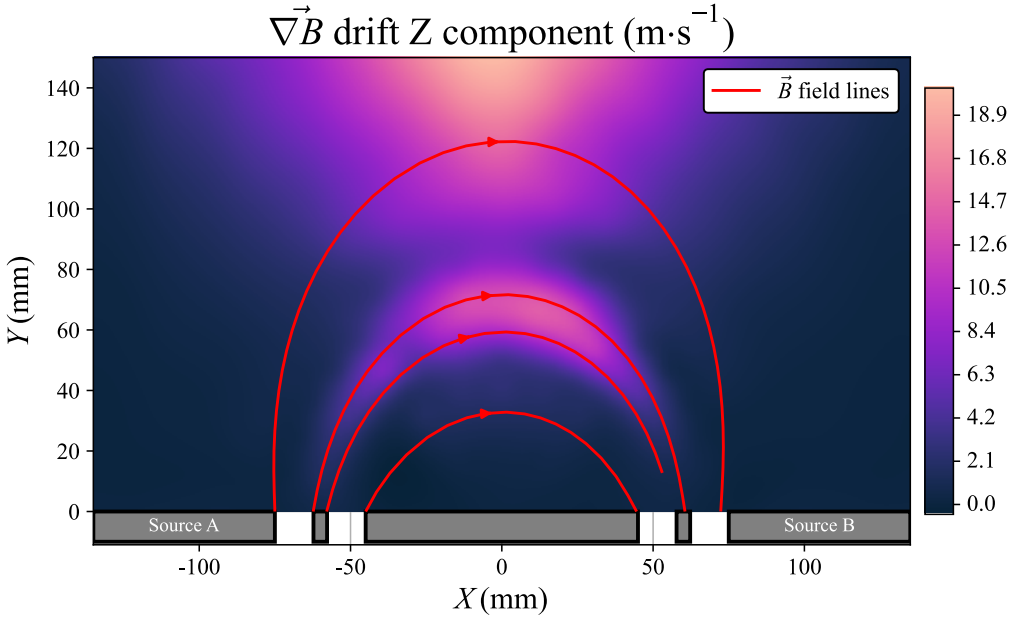

Figure 4.21: Vertical speed of the $\nabla\vec{B}$ drift.

Since the magnetic field intensity is decreasing downstream of the thruster, the presence of a $\nabla\vec{B}$ drift is expected. The vertical component of the drift velocity of electrons is displayed on fig.4.21. The value of the kinetic energy of the electrons is obtained using the electron temperature and assuming an isotropic thermal velocity. As seen on fig.4.21 the arch between the antenna streamlines presents high positive values of the drift velocity, due to the high electron temperature at this location. The drift velocities are in the same order of magnitude as for the $\vec{E} \times \vec{B}$ drift and point in the same direction, towards the top of the thruster. The $\nabla\vec{B}$ is thus another candidate to explain the asymmetry. However, the low velocity values suggest that it is not the only contributor.

4.5.4 $\vec{B}$ curvature drift

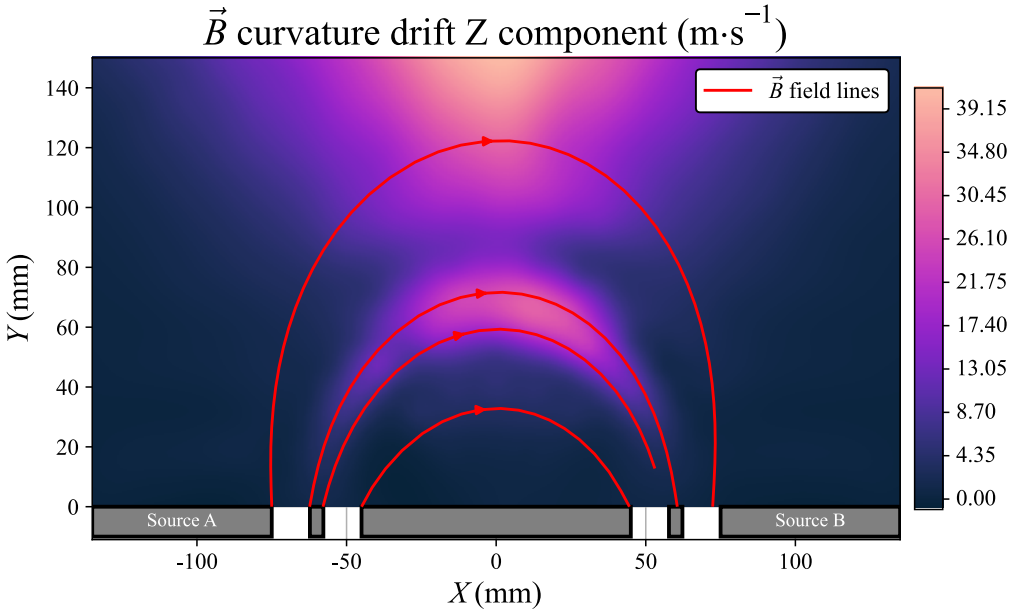

Figure 4.22: Vertical speed of the $\vec{B}$ curvature drift.

The curvature drift is another candidate to explain the asymmetry, since the magnetic arch configuration is characterized by its curved arch in the exhaust region. The vertical drift velocities are computed for the electrons and plotted in fig.4.22. Similarly to the $\nabla\vec{B}$ drift, the energy is obtained by the same assumptions. The spatial distribution of the $\vec{B}$ curvature drift is very similar to the $\nabla\vec{B}$ drift, with velocity values twice as important. Here again, the velocities are in the same order of magnitude, which are too slow to explain the asymmetry on their own.
As the magnetic arch configuration presents a magnetic mirror along the streamlines, it is possible for electrons to bounce back and forth inside the arch completing several roundtrips between the sources. As those confined electrons remain longer in the arch region, they could be deviated upwards as they experience the drift forces for a longer time.
Considering the combination of the three drift phenomenons, we have electrons being deviated towards the top in all three cases, which is coherent with the observations on fig.4.14.
Also, the drift velocities change sign if the magnetic field is reversed which matches the observed reversal of the asymmetry in the reversed magnetic field configuration (see fig.4.17).

4.6 Thermal analysis

As mentioned in 3.1.2, the temperatures of critical parts of the thruster and transmission line were monitored using thermocouples. While the primary purpose of the temperature monitoring was to avoid damaging the elements of the transmission line, temperature data from the thermocouples contains valuable information to be used for thermal analysis of the plasma chambers.
According to the observed temperature data, the three-way splitter heats up immediately when the microwave generator is turned on, by analyzing the data, the total operating time of the thruster is computed to be 11 hours 17 minutes over the whole experimental campaign.

The losses at the wall can also be estimated, although with high uncertainties as the thermocouples were not directly connected to the chamber walls, but to the 7/16 connectors upstream of the chambers (see fig.3.2). By obtaining the heating rate of the thermocouples at low temperature (where radiative losses can be neglected), knowing the transmitted microwave power and the mass of the chambers a simple calculation can be performed based on a 0-D model.

The transmission line characteristics in tab.3.1 are exploited to compute a total loss of 28%. The mass of the metallic components connected to the connector are summed to obtain the total mass and a heat capacity of 505 $J \cdot kg^{-1} \cdot K^{-1}$ is considered for the 316L stainless steel.
Losses of the order of 22% are obtained. Since the model used is very simple and the temperature is obtained far upstream of the chamber and the thermal conductivity of the components isn't perfect, the real value of thermal losses should be considered higher than what is found, possibly double.

Chapter 5

Conclusion

5.1 Outcomes of the work performed

In conclusion, a thorough investigation of the exhaust plume of the magnetic arch thruster was performed. The magnetic field generated by the permanent magnets and the coils was accurately measured and the results were exploited to support the analysis of the plasma measurements. The ion current density and IEDF were measured in both the horizontal and vertical plane of the thruster at several operating points. Building on the results of those measurements, key operating points were selected to perform Langmuir probe scans of the plume in both planes. Those scans allowed to obtain the following plasma parameters V_p, V_f, T_e, N_i, N_e, λ_D in the exhaust plume and magnetic arch.
Those measurements are the first to fully (in 2D rather than along a single line) characterize the exhaust plume of cluster of ECRTs in a magnetic arch configuration. They provide valuable information on the behavior of the plasma in the presence of a magnetic arch. The measurements performed in the vertical plane, perpendicular to the exhaust plane of the thruster, revealed the presence of asymmetries initially observed visually. Hypothesis were formulated to explain the reason behind those asymmetries and are qualitatively coherent with the measurements. Data and experiments shows that it is certain that the asymmetries are dependent on the field's orientation and are likely caused by drift phenomenons.
About the plasma physics inside the magnetic arch, results show that the electrons remain essentially magnetized along the streamlines origination from the antennas and acquire high temperatures, possibly ionizing neutrals inside the arch region. This is due both to the magnetic mirror present in the magnetic arch and to the plasma wave coupling being stronger close to the antenna, where the electric field of the microwaves is stronger. The strong magnetization of electrons prevents them from efficiently escaping the magnetic arch and creating a strong enough ambipolar field, thus explaining the relatively low plasma potential drop and low energy ions measured by the RPA. Additionally, ions which are still weakly magnetized, may also be slowed down by the arch, instead of being accelerated purely downstream.

5.2 Thruster optimization pathways

The results show that the sources are relatively inefficient at ionizing and accelerating the plasma, this is suspected to be caused by considerable losses at the plasma chambers walls. In order to reduce those losses, several actions could be taken. The plasma chambers could be redesigned to be shallower, this alone would reduce the amount of electrons lost to the wall due to streamlines originating from the ECR region intersecting chamber walls downstream.
Another option would be to modify the location of the gas injection ring, making its radius smaller would lead to the propellant being injected closer to the antenna, where electrons are heated most efficiently and the furthest away from the chamber walls. This could be achieved by making the external ceramic with a smaller internal diameter and shortening the internal ceramic by half (see fig.3.2). In this way the gas would be injected directly around the antenna.
Another way of improving the source efficiency is to thicken the ECR region [39], this could be achieved passively by using ferromagnetic material at judicious locations around the chamber.

In order to improve the repeatability of thruster's performances, the gas could be independently injected in each source using 2 mass flow controllers. This would eliminate the mass flow uncertainty induced by the use of a gas splitter. The thermal monitoring could gain in accuracy by piercing a hole inside the chamber wall to lodge a thermocouple and access the chamber wall temperature directly. During the experimental campaign, the thermocouples were placed behind the chamber at the 7/16 connector, inducing delay and increased uncertainty in temperature measurements.
Cooling could be implemented for two reasons, first to allow longer operation times and shorten experimental campaigns, second to control the thruster equilibrium temperature and take into account the possible effects of temperature on the performances. The cooling could be achieved simply with heat pipes connecting the chambers to a massive metal bloc, or through conformal water cooling of the chambers for a more efficient but complex solution.

5.3 Future work on the magnetic arch thruster

In this work, the operating parameters were limited to varying the mass flow rate of Xenon and the microwave power, the magnetic field inside the arch was set to a unique configuration. It would be interesting to explore the effect of the magnetic arch shape on the performances. Several options could be studied, by varying the field applied to the coils, the ECR region would change location inside the chamber and the topology of the magnetic arch would change, by applying asymmetric fields to the coils (one stronger than the other), the exhaust plume could be oriented to achieve thrust vectoring.
While it requires a heavy redesign of the thruster, having a variable distance between the sources and controlling their orientation could lead to improvements in plasma detachment and thus efficiency.

Bibliography

[1] Mario Merino et al. "Electrodeless Plasma Thruster research within the ERC-ZARATHUSTRA project". In: *Proceedings of the Electric Rocket Propulsion Society (IEPC 2025)*. Paper IEPC-2025-322. London, United Kingdom, 2025. URL: https://virtual.oxfordabstracts.com/event/73412/submission/322.

[2] NanoAvionics. *How many satellites are in space?* Accessed: 2025-05-23. 2024. URL: https://nanoavionics.com/blog/how-many-satellites-are-in-space/?utm_source=chatgpt.com.

[3] J. H. Saleh et al. "Electric propulsion reliability: statistical analysis of on-orbit anomalies and comparative analysis of electric versus chemical propulsion failure rates". In: *arXiv preprint arXiv:1706.10129* (2017). URL: https://arxiv.org/abs/1706.10129.

[4] Financial Times. *A new space race: the satellite surge and its business implications*. Accessed: 2025-05-23. 2023. URL: https://www.ft.com/content/b635423f-e721-454c-b75c-98d0ad8fedf1.

[5] Wired. *Ion Propulsion Helps Spacecraft Cruise Solar System on the Cheap*. Accessed: 2025-05-23. 2007. URL: https://www.wired.com/2007/10/ion-propulsion-helps-spacecraft-cruise-solar-system-on-the-cheap/.

[6] European Space Agency. *SMART-1 Mission Overview*. Accessed: 2025-05-23. URL: https://www.esa.int/Science_Exploration/Space_Science/SMART-12.

[7] Wikipedia contributors. *Hayabusa2 — Wikipedia*. Accessed: 2025-05-23. URL: https://en.wikipedia.org/wiki/Hayabusa2.

[8] Wikipedia contributors. *Hall-effect thruster — Wikipedia*. Accessed: 2025-05-23. 2025. URL: https://en.wikipedia.org/wiki/Hall-effect_thruster.

[9] Wikipedia contributors. *Ion thruster — Wikipedia*. Accessed: 2025-05-23. URL: https://en.wikipedia.org/wiki/Ion_thruster.

[10] Wikipedia contributors. *Electrodeless plasma thruster — Wikipedia*. Accessed: 2025-05-23. URL: https://en.wikipedia.org/wiki/Electrodeless_plasma_thruster.

[11] J. Navarro-Cavallé M. Merino C. Boyé. "Experimental analysis of a magnetic arch configuration for ECR plasma thrusters". In: *Frontiers in Physics* 13.44205 (2025). DOI: 10.1007/s44205-025-00100-w. URL: https://link.springer.com/article/10.1007/s44205-025-00100-w.

[12] Simone Di Fede et al. "Magnetic nozzle performance in a cluster of Helicon Plasma Thrusters". In: *Plasma Sources Science and Technology* 32.6 (2023), p. 065013. DOI: 10.1088/1361-6595/acdaf2.

[13] C. Boyé, J. Navarro-Cavallé, and M. Merino. "Ion current and energy in the Magnetic Arch of a cluster of two ECR plasma sources". In: *Journal of Electric Propulsion* 4.1 (2025). DOI: 10.1007/s44205-025-00100-w.

[14] Célian Boyé et al. "Determining ion velocity in the interconnected plume of a cluster of two ECRTs using 2D LIF". In: *Electric Rocket Propulsion Society - IEPC 2024 proceedings*. Electric Rocket Propulsion Society - IEPC 2024 proceedings. Toulouse, France, 2024, IEPC 2024–717. URL: https://hal.science/hal-04686118.

[15] Edgar Choueiri. "A critical history of electric propulsion: The First Fifty Years (1906-1956)". In: *40th AIAA/ASME/SAE/ASEE Joint Propulsion Conference and Exhibit* (2004). DOI: 10.2514/6.2004-3334.

[16] Dan M. Goebel and Ira Katz. *Fundamentals of electric propulsion: Ion and hall thrusters*. Wiley, 2008.

[17] P.K. Lebedev and V.I. Pryanichnikov. "Present and future production of Xenon and Krypton in the former USSR region and some physical properties of these gases". In: *Nuclear Instruments and Methods in Physics Research Section A: Accelerators, Spectrometers, Detectors and Associated Equipment* 327.1 (1993), pp. 222–226. DOI: 10.1016/0168-9002(93)91447-u.

[18] Adam Shabshelowitz. "Study of RF Plasma Technology Applied to Air-Breathing Electric Propulsion." PhD thesis. University of Michigan, 2013.

[19] Hai-Xing Wang, Su-Rong Sun, and Wei-Ping Sun. "Status and prospects on nonequilibrium modeling of high velocity plasma flow in an Arcjet thruster". In: *Plasma Chemistry and Plasma Processing* 35.3 (2015), pp. 543–564. DOI: 10.1007/s11090-015-9610-4.

[20] Filippo Alifano, Mario Panelli, and Francesco Battista. "Preliminary Design Tool for Medium-Low-Power Gridded Ion Thrusters". In: *Applied Sciences* 13 (2023), p. 5600. DOI: 10.3390/app13095600.

[21] Princeton Plasma Physiscs Laboratory. *Hall Thrusters*. URL: https://htx.pppl.gov/thrusters.html.

[22] ScienceDirect. URL: https://www.sciencedirect.com/topics/engineering/pulsed-plasma-thrusters.

[23] Thomas F. Munro-O'Brien and Charles N. Ryan. "Performance of a low power Hall effect thruster with several gaseous propellants". In: *Acta Astronautica* 206 (2023), pp. 257–273. ISSN: 0094-5765. DOI: https://doi.org/10.1016/j.actaastro.2023.01.033. URL: https://www.sciencedirect.com/science/article/pii/S0094576523000449.

[24] Wikipedia contributors. *Debye length*. Accessed: 2025-05-29. 2025. URL: https://en.wikipedia.org/wiki/Debye_length.

[25] A. Kramida et al. *NIST Atomic Spectra Database (version 5.11)*. https://physics.nist.gov/asd. National Institute of Standards and Technology, Gaithersburg, MD. 2023. DOI: 10.18434/T4W30F.

[26] PIE Scientific LLC. *ECR (Electron Cyclotron Resonance) Plasma Source*. Accessed: 2025-05-29. 2024. URL: https://piescientific.com/resource_pages/resource_ecr_plasma/.

[27] Robert B. Lobbia and Brian E. Beal. "Recommended practice for use of Langmuir probes in electric propulsion testing". In: *Journal of Propulsion and Power* 33.3 (2017), pp. 566–581. DOI: 10.2514/1.b35531.

[28] Francis F. Chen. *Francis F. Chen - Lecture notes on langmuir probe diagnostics*. 2003. URL: https://www.scribd.com/document/95164905/Francis-F-Chen-Lecture-Notes-on-Langmuir-Probe-Diagnostics.

[29] E.D. Cantero et al. "Design of a compact Faraday cup for low energy, low intensity ion beams". In: *Nuclear Instruments and Methods in Physics Research Section A: Accelerators, Spectrometers, Detectors and Associated Equipment* 807 (2016), pp. 86–93. ISSN: 0168-9002. DOI: https://doi.org/10.1016/j.nima.2015.09.096. URL: https://www.sciencedirect.com/science/article/pii/S0168900215011675.

[30] Stéphane Mazouffre. "Electric propulsion for satellites and spacecraft: Established Technologies and novel approaches". In: *Plasma Sources Science and Technology* 25.3 (2016), p. 033002. DOI: 10.1088/0963-0252/25/3/033002.

[31] Nina Henrich et al. "Retarding Potential Analyser Development for Low Density FEEP Thruster Beam Diagnostics". In: *Electric Rocket Propulsion Society - IEPC 2019 proceedings*. 2019.

[32] R.W. Boswell. "Plasma production using a standing helicon wave". In: *Physics Letters A* 33.7 (1970), pp. 457–458. ISSN: 0375-9601. DOI: https://doi.org/10.1016/0375-9601(70)90606-7. URL: https://www.sciencedirect.com/science/article/pii/0375960170906067.

[33] Federico Boni, Victor Désangles, and Julien Jarrige. "Experimental characterization of thrust production mechanisms in a magnetic nozzle ECR thruster". In: *Journal of Electric Propulsion* 1.1 (2022). DOI: 10.1007/s44205-022-00034-7.

[34] EP2 Research Group. *EP2ResearchGroup*. URL: https://ep2.uc3m.es/.

[35] Anna J. Sheppard and Justin M. Little. "Performance analysis of an electron cyclotron resonance thruster with various propellants". In: *Journal of Propulsion and Power* 38.6 (2022), pp. 998–1008. DOI: 10.2514/1.b38698.

[36] MR Inchingolo et al. "Thrust measurements of a waveguide electron cyclotron resonance thruster". In: *Journal of Applied Physics* 135.9 (2024).

[37] F Cannat et al. "Optimization of a coaxial electron cyclotron resonance plasma thruster with an analytical model". In: *Physics of Plasmas* 22.5 (2015).

[38] Clara Schäfer et al. "INVESTIGATION OF MICROWAVE COUPLING AND MAGNETIC FIELD TOPOLOGY EFFECTS ON ION ENERGY IN TWO THRUSTER CONCEPTS". In: *9th Edition of the 3AF International Conference on Space Propulsion 2024*. 2024, pp. 1–9.

[39] Clara Schäfer. "Impact of Microwave Coupling and Magnetic Field Topology on Thrust and Beam Parameters in Electron Cyclotron Resonance Thrusters with Magnetic Nozzles". PhD thesis. Justus-Liebig-Universität Gießen, 2025.

[40] Oliver Hitchens. "Performance increase of electron cyclotron resonance magnetic nozzle thruster via magnetically thickened resonance region". PhD thesis. University of Surrey, 2025.

[41] Frans Ebersohn et al. "Magnetic nozzle plasma plume: review of crucial physical phenomena". In: *48th AIAA/ASME/SAE/ASEE Joint Propulsion Conference & Exhibit*. 2012, p. 4274.

[42] Leybold. *Space simulation systems Univex Leybold*. URL: https://www.leybold.com/en/products/systems-and-solutions/space-simulation-systems.

[43] Qian Y. Jin et al. "RF and Microwave Ion Sources Study at Institute of Modern Physics". In: *Plasma* 4.2 (2021), pp. 332–344. ISSN: 2571-6182. DOI: 10.3390/plasma4020022. URL: https://www.mdpi.com/2571-6182/4/2/22.

Appendix A

Appendix

A.1 DAQ program & hardware

The acquisition of the measurements for the magnetic field of the thruster was automatized via a LabVIEW program then executed by a 3 degrees od freedom arm system developed in house by EP2 Laboratory. The program responsible for the robotic arm movement was developed by Dr. Macro Inchigolo, the sub-program for Gauss probe data acquisition was developed by the author.The LabVIEW front panel, block diagram and the arm system are presented on fig.A.1, fig.A.2 and fig.A.3 respectively.

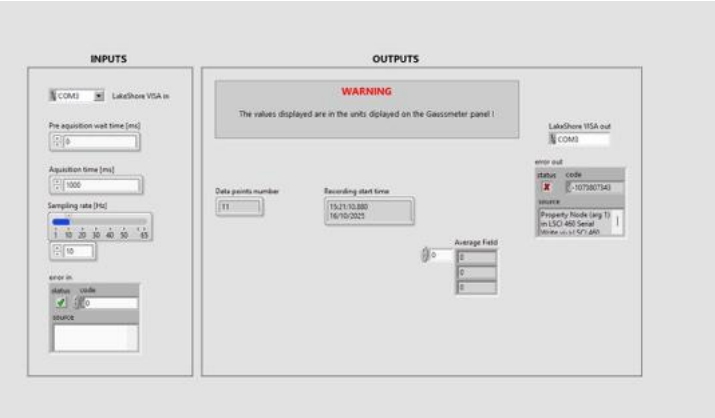

Figure A.1: LabVIEW sub VI front panel for Gauss probe data acquisition.

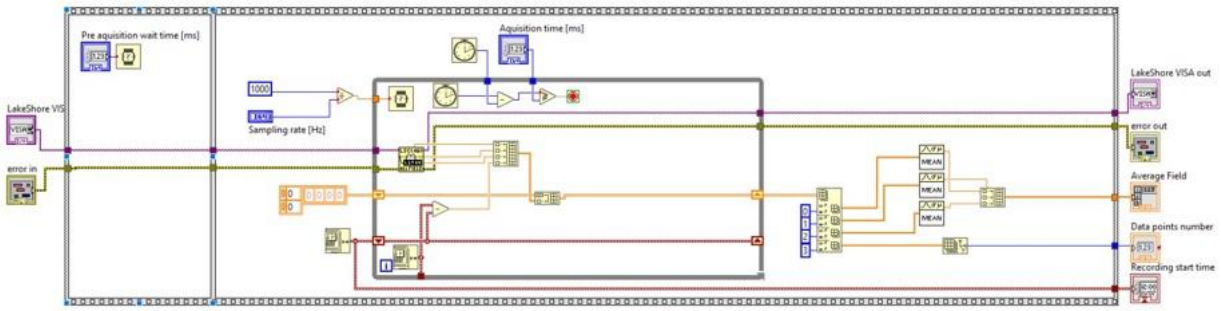

Figure A.2: LabVIEW sub VI block diagram for Gauss probe data acquisition.

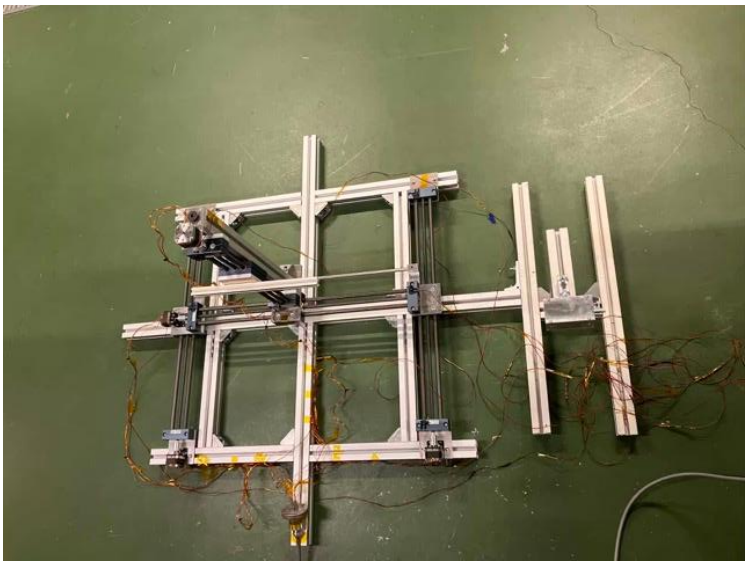

Figure A.3: Photograph of the 3 degrees of freedom arm system used for magnetic field measurements.

A.2 Thermal monitoring

As mentioned in 3.1.2, the temperatures of key elements of the transmission line were monitored with thermocouples using the *Picolog* software. An example of the temperature data over one day of the experimental campaign is provided in fig.A.4.
Notice the rapid increase in temperature and the long cooling times.

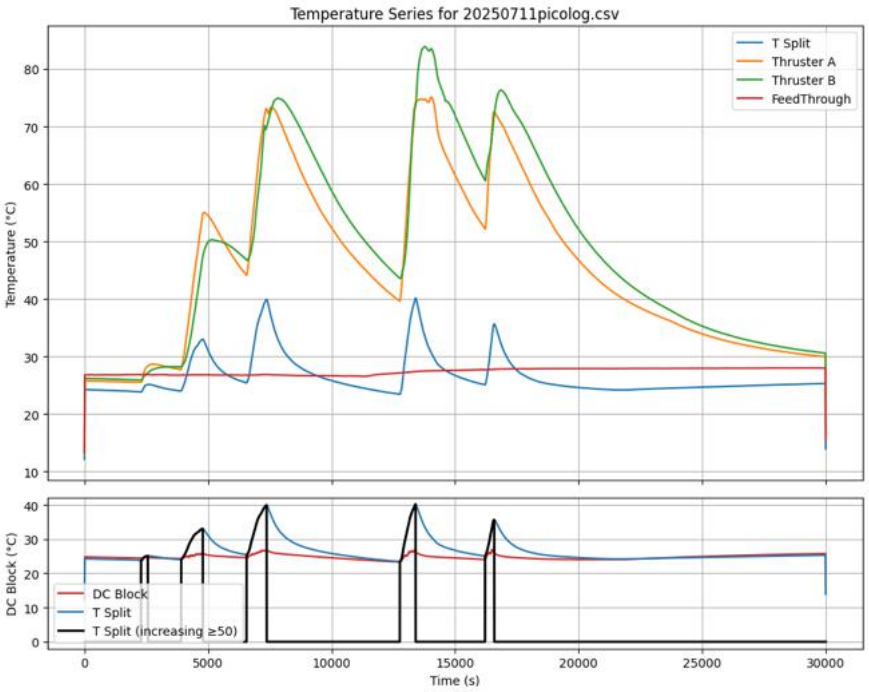

Figure A.4: Temperature series of the transmission line.

A.3 Ceramics degradation

The photographs of the external ceramics after the experimental campaign (11-hour in total) are shown in fig.A.5. One can clearly notice the beige deposit on the front side (left one in the figure) caused by plasma exposure. The outer rim remains white, as it is shielded from the plasma by the metallic plasma chamber piece. The backside ceramic (right one in the figure) appears cleaner; however, its inner region also shows some deposits, although less visible. This suggests that plasma may also form behind the ceramics, near the gas injection region. Another possibility is that energetic ions travel through the annular gap between the ceramics and erode the metal parts behind them, leading to etching and subsequent deposition on the rear surface. Refer to fig.3.2 for the CAD model of the plasma chamber.
Both ceramic pieces show dark marks resulting from friction with the metal during assembly and disassembly of the thruster. They also both exhibit cracks, which were already present before the experimental campaign and were repaired with ceramic paste prior to testing.

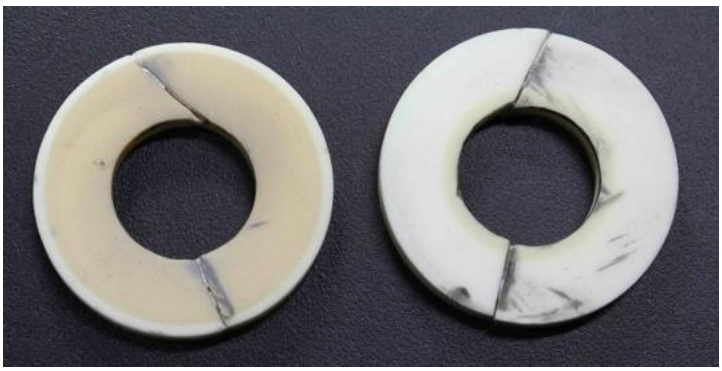

Figure A.5: Photograph of the external ceramics after the experimental campaign: plasma exposed front side (left) and backside (right).

Photographs of the internal ceramics after the experimental campaign (11-hour operation in total) are shown in fig.A.6.
A similar beige deposit can be observed on the front side of the internal ceramics, which are directly exposed to the plasma. The inner region, close to the central hole where the antenna is located, presents a darker and more intense deposit. This is likely due to the close proximity to the antenna, from which metallic material is probably sputtered.
On the back side, a comparable deposit can be seen, except for the inner area that is protected by the 7/16 connector. This suggests that plasma may also be generated upstream of the chamber, between the internal ceramic and the coaxial cable, i.e., inside the 7/16 connector. Although the CAD model suggests that this region should be inaccessible to the propellant gas, tolerances in the internal ceramic dimensions and the practical assembly of the thruster can lead to small gaps allowing gas flow (see fig.3.2). Measurements performed with the Gauss probe (independent from the scan in 4.1) indicate that another ECR region at approximately 875 G is present inside the 7/16 connector, supporting this hypothesis. The presence of a similar beige deposit on the ceramic of the coaxial cable connected to the plasma sources further corroborates this observation (see fig.A.7). Such a phenomenon would lead to additional thermal and efficiency losses.



Figure A.6: Photograph of the internal ceramics after the experimental campaign: plasma exposed front side (left) and backside (right).



Figure A.7: Photograph of the coaxial cable's ceramic (cable's end connected to the plasma source) after the experimental campaign.